

The dependence of subhalo abundance matching on galaxy photometry and selection criteria

Richard Stiskalek^{1,2,3*}, Harry Desmond^{1†}, Thomas Holvey¹ and Michael G. Jones^{4,5}

¹*Department of Physics, University of Oxford, Denys Wilkinson Building, Keble Road, Oxford OX1 3RH, UK*

²*Fakultät für Physik, Ludwig-Maximilians-Universität München, 80333 München, Germany*

³*School of Physics and Astronomy, University of Glasgow, Glasgow G12 8QQ, UK*

⁴*Instituto de Astrofísica de Andalucía (IAA-CSIC), Glorieta de la Astronomía s/n, 18008, Granada, Spain*

⁵*Steward Observatory, University of Arizona, 933 North Cherry Avenue, Rm. N204, Tucson, AZ 85721-0065, USA*

Last updated xxx Xxx x; in original form xxx Xxx x

ABSTRACT

Subhalo abundance matching (SHAM) is a popular technique for assigning galaxy mass or luminosity to haloes produced in N -body simulations. The method works by matching the cumulative number functions of the galaxy and halo properties, and is therefore sensitive both to the precise definitions of those properties and to the selection criteria used to define the samples. Further dependence follows when SHAM parameters are calibrated with galaxy clustering, which is known to depend strongly on the manner in which galaxies are selected. In this paper we introduce a new parametrisation for SHAM and derive the best-fit SHAM parameters as a function of various properties of the selection of the galaxy sample and of the photometric definition, including Sérsic vs Petrosian magnitudes, stellar masses vs r -band magnitudes and optical (SDSS) vs H α (ALFALFA) selection. In each case we calculate the models' goodness-of-fit to measurements of the projected two-point galaxy correlation function. In the optically-selected samples we find strong evidence that the scatter in the galaxy–halo connection increases towards the faint end, and that AM performs better with luminosity than stellar mass. The SHAM parameters of optically- and H α -selected galaxies are mutually exclusive, with the latter suggesting the importance of properties beyond halo mass. We provide best-fit parameters for the SHAM galaxy–halo connection as a function of each of our input choices, extending the domain of validity of the model while reducing potential systematic error in its use.

Key words: galaxies: haloes – cosmology: dark matter – galaxies: photometry

1 INTRODUCTION

Currently, our best tool to understand the growth of structure in the Universe is simulation of dark matter halo formation and evolution. While cosmological hydrodynamical simulations have increased greatly in sophistication in the past decade, the complexity of baryonic processes means that simulations of the gravitational physics of dark matter only (N -body simulations) remain the most robust, with broad consensus on the resulting halo population across the range of algorithms that have been used (Navarro et al. 1997; Knebe et al. 2011; Schneider et al. 2016). To connect such simulations to observations, empirical and semi-analytic models have been developed to associate galaxies with the simulated haloes and track the coevolution of the two over cosmic time. These models vary considerably in complexity and scope, ranging from simple parametrised prescriptions for relating galaxy and halo properties (e.g. the Halo

Occupation Distribution; Kravtsov et al. 2004; Zheng et al. 2005; Skibba & Sheth 2009) to fully probabilistic models of galaxy formation as a function of halo mass accretion histories (Moster et al. 2018; Behroozi et al. 2019; O’Leary et al. 2020).

A model towards the empirical end of this spectrum is abundance matching (AM), which is a simple and versatile prescription for the galaxy–halo connection. In its most basic form, AM assumes a monotonic relation between halo mass and galaxy mass or luminosity, such that the brightest galaxy within a given survey volume is associated with the most massive halo produced in a similar volume of an N -body simulation, the next brightest with the next most massive and so on down the list (Kravtsov et al. 2004; Vale & Ostriker 2004; Conroy et al. 2006; Behroozi et al. 2010; Moster et al. 2010). The method has subsequently been extended to incorporate subhaloes (SHAM) and scatter in the relation between galaxies and haloes, and to vary the halo property used as the “proxy” for galaxy mass (Behroozi et al. 2010; Reddick et al. 2013; Chaves-Montero et al. 2016; Lehmann et al. 2017). While reproducing the stellar mass function (SMF) or stellar luminosity function (LF) by construction,

* richard.stiskalek@protonmail.com

† harry.desmond@physics.ox.ac.uk

SHAM has been shown to give good predictions for galaxy clustering and satellite fractions as a function of mass (e.g. Conroy et al. 2006; Reddick et al. 2013; Lehmann et al. 2017), and to be able to explain aspects of galaxy dynamics (Desmond & Wechsler 2015, 2017; Desmond 2017). This suggests that SHAM encapsulates important physics regarding the processes of galaxy formation, and also makes it useful for cosmological studies that require the galaxy–halo connection as input (e.g. Reddick et al. 2014).

With galaxy correlation function as the main observable that has been used so far to test and constrain SHAM, the model is sensitive to effects that impact galaxy clustering. A systematic study of such effects on the results of SHAM is however lacking. In particular, previous studies have taken for granted both survey selection criteria and photometric modelling choices, both of which are known to impact the inputs to SHAM. The galaxy data most commonly used for SHAM derives from the Sloan Digital Sky Survey (SDSS)¹, with previous studies typically preferring the Petrosian photometry pipeline from the New York University Value Added Galaxy Catalog (NYU-VAGC)² (Blanton et al. 2005). The selection here is done mainly on the basis of r -band magnitude, tracing main sequence stars. Galaxies selected through emission at other wavelengths, e.g. 21cm (HI), are much more weakly clustered (Li et al. 2012; Martin et al. 2012; Papastergis et al. 2013). This requires SHAM models designed for such samples to associate galaxies with a subset of the halo population significantly biased in quantities that affect clustering, for example formation time (Guo et al. 2017).

The photometric pipeline used to reduce the raw images also has an impact on the luminosities and stellar masses derived. There has been much discussion in the literature as to the best method for determining these, both as regards the luminosity in the low surface brightness outer regions of galaxies (Blanton et al. 2011; Bernardi et al. 2013; Kravtsov et al. 2018) and the method used to convert galaxy fluxes and spectra to stellar masses (Baldry et al. 2008 and references therein). Since these affect the LF and SMF, they alter the galaxy correlation functions produced by a given SHAM model, and hence the best-fit parameters of SHAM itself.

The stellar-to-halo mass relation has been extensively studied, with evidence accruing for an intrinsic scatter around 0.2 dex (e.g. Behroozi et al. (2010); Moster et al. (2010); Rodríguez-Puebla et al. (2011)). The stellar-to-halo mass relation of simulated faint galaxies was studied in Munshi et al. (2021), finding an increasing scatter in the relation towards the lower-mass halos. Likewise, To et al. (2020) constrained the luminosity scatter at a fixed halo mass of red galaxies, finding similar values of scatter as in the stellar-to-halo-mass relation. On the other hand, the relation between the gas mass of a galaxy and halo properties is relatively little constrained; there may even be a non-monotonic relation between the two (e.g. Guo et al. 2017). This agrees with the direct measurement of the $M_{\text{HI}}-M_h$ relation of Guo et al. (2020), who found that only the satellite HI mass increases monotonically with halo mass. Chauhan et al. (2020) also found a non-monotonic $M_{\text{HI}}-M_h$ relation, and studied the physical drivers of the relation in a semi-analytic galaxy formation model. Lu et al. (2020) developed an empirical model for HI mass distribution within dark matter halos using galaxy group catalogues, and used it to predict HI masses and satellite fractions. A non-monotonic $M_{\text{HI}}-M_h$ relation was also found in Calette et al. (2021), who first impose a stellar mass–circular velocity relation via

SHAM and then use an empirical HI–stellar mass relation to predict the galaxy HI content.

In this paper, we explore the impact of both photometric pipeline and selection criteria on the results and the best-fit parameters of SHAM. In particular, we will consider both optically selected galaxies from the NYU-VAGC and Nasa Sloan Atlas (NSA)³, and HI-selected galaxies from the ALFALFA HI survey (Giovanelli et al. 2005, 2007; Saintonge et al. 2008; Haynes et al. 2018)⁴, in a matched catalogue. For the galaxy property used in SHAM, we will consider both the Sérsic and Petrosian (two-dimensional, i.e. elliptical, in the case of the NSA) magnitudes along with their corresponding stellar mass estimates. Sérsic magnitudes derive from fitting a Sérsic profile (Sérsic 1968) to the surface brightness profiles of galaxies, while the Petrosian magnitude is the flux from within the Petrosian radius where the surface brightness is a fixed fraction of the mean surface brightness within that radius (Petrosian 1976). For each one we compute the luminosity and stellar mass functions, and the correlation functions in bins. We fit an SHAM model in each case, deriving constraints on the SHAM parameters and calculating the goodness-of-fit of the model by means of the Bayesian evidence. This will let us answer the following questions:

- How do the best-fit SHAM parameters vary with galaxy magnitude or stellar mass?
- Is there consistency between SHAM results for different photometric pipelines and selection criteria; or, more generally, how do the inferred SHAM parameters depend on these?
- Which of the above is most suitable for doing SHAM in the sense of maximising goodness-of-fit of the model?
- What are the differences between SHAM based on M_r vs M_* , and for which does SHAM provide the best fit?
- How do the two-point correlation functions, LFs and, SMFs differ between r -band and HI-selected samples, and how does this impact the results of SHAM?

Our aim is therefore to determine both how well SHAM works under various conditions, and the sensitivity of its parameters to galaxy sample and systematic effects in galaxy modelling. We anticipate this to prove useful for understanding the physical significance of the model, and for ensuring that it is as accurate as possible for specific science applications. We work in the context of a custom-built SHAM model that is however similar to those in the literature (especially Lehmann et al. 2017), as we describe fully in Sec. 3.1. Within the SHAM framework, we match galaxies to both haloes and subhaloes. Unless an explicit distinction is drawn, we refer to both haloes and subhaloes collectively as “haloes”. We assume a flat Λ CDM model with a matter density parameter of $\Omega_m = 0.295$ and quote results assuming a Hubble constant $H_0 = 70 \text{ km s}^{-1} \text{ Mpc}^{-1}$, unless $h \equiv H_0/(100 \text{ km s}^{-1} \text{ Mpc}^{-1})$ is explicitly mentioned. All logarithms are base-10. We make our code publicly available.⁵

The structure of the paper is as follows. Sec. 2 documents the observed and simulated data that we use. Sec. 3 describes our methodology, including SHAM modelling, calculation of correlation functions, and the likelihood framework for inferring SHAM parameters and testing goodness-of-fit. Sec. 4 presents our results, Sec. 5 discusses the broader impact of our study and suggests avenues for further work, and finally Sec. 6 concludes.

¹ <https://www.sdss.org/>

² <http://sdss.physics.nyu.edu/vagc/>

³ <http://nsatlas.org/>

⁴ <http://egg.astro.cornell.edu/index.php/>

⁵ github.com/Richard-Sti/ClusterSHAM

2 OBSERVED AND SIMULATED DATA

2.1 Observational data

We study three galaxy catalogues. The first, the NYU-VAGC⁶, is based on the SDSS DR7 (York et al. 2000; Abazajian et al. 2009; Eisenstein et al. 2001), consisting of 7966 deg² of spectroscopic coverage. We use the NYU-VAGC Petrosian model magnitudes K-corrected to $z = 0.0$ (Blanton & Roweis 2007), and select galaxies with apparent r -band magnitude $10 < m_r < 17.7$ and redshift $0.01 < z < 0.15$ from the NYU-VAGC large-scale structure sample.⁷ The lower redshift limit excludes nearby galaxies whose redshift estimate may be dominated by peculiar velocities. Despite the fact that NYU-VAGC extends significantly beyond $z = 0.15$ we opt for this upper limit to ensure fair comparison with the NSA, which only extends to $z = 0.15$.

The second catalogue we use is the NSA, a database of images and parameters of local galaxies based primarily on results from the SDSS DR13 (Albareti et al. 2017) and the Galaxy Evolution Explorer (Martin et al. 2005). v1_0_1 of the NSA⁸ contains 641,409 galaxies up to $z = 0.15$. The NSA includes elliptical Petrosian and Sérsic aperture photometry fits K-corrected to $z = 0.0$, both of which we use in our analysis. Based on simulations, the elliptical Petrosian photometry avoids biases present in the Sérsic photometry and is, therefore, considered more reliable. We again limit the apparent r -band magnitude to $10 < m_r < 17.6$ and use the same redshift cuts as for the NYU-VAGC. Furthermore, we only select galaxies which are also present in the NYU-VAGC large-scale structure sample. Both the NYU-VAGC and NSA galaxy catalogues are corrected for fibre collisions: fibre collided galaxies, which would otherwise lack redshifts, are assigned the nearest neighbour’s redshift (Stoughton et al. 2002; Zehavi et al. 2005).

Our final galaxy catalogue consists of optically-selected NSA and HI-selected galaxies from ALFALFA, a blind, second generation extragalactic HI survey. The full ALFALFA catalogue, denoted $\alpha.100$, contains $\sim 31,500$ HI line sources up to $z = 0.06$ with HI masses ranging from 10^6 to $10^{10.8} M_\odot$ (Haynes et al. 2018). We include both code 1 and code 2 ALFALFA sources; although the completeness of the survey is different between these, our method for determining the correlation functions (Sec. 3.3) applies equally to both of them. ALFALFA has a partial overlap with SDSS, allowing for matching between the two surveys. We begin with the SDSS match performed in Durbala et al. (2020). We then match the position of the optical counterpart to the sources in the Nasa Sloan Atlas using an on-sky angle tolerance of $5''$ and a line-of-sight distance tolerance of 10 Mpc. These fairly stringent criteria yield a low probability of mismatches and hence a high sample purity, while still retaining 21,776 galaxies. We restrict the footprint of the combined catalogue to the “Spring” section of the ALFALFA footprint⁹ to avoid regions of poor coverage in SDSS, which removes $\sim 15\%$ of the total survey area. Of the remaining HI sources with optical counterparts, 83.6% have stellar mass estimates in the NSA (9,802 galaxies). The missing galaxies are mainly nearby and with low HI mass. We will locate galaxies in the matched catalogue using the sky coordinates and redshift quoted in the NSA.

⁶ <http://sdss.physics.nyu.edu/vagc/>

⁷ <http://sdss.physics.nyu.edu/vagc/lss.html>

⁸ <https://www.sdss.org/dr13/manga/manga-target-selection/nsa/>

⁹ http://egg.astro.cornell.edu/alfalfa/scheds/status_spr11.php

2.2 Simulation data

We base our SHAM mock catalogues on the DarkSky simulation¹⁰ (Skillman et al. 2014). In particular we use the DarkSky 400 Mpc/ h box (ds14_i_4096) run with 2HOT code (Warren 2013) and 4,096³ particles. The particle mass is $7.63 \times 10^7 M_\odot/h$, and the minimum halo virial mass in the catalogue is $3 \times 10^9 M_\odot/h$, corresponding to ~ 40 particles. In the subsequent analysis we ensure that the haloes matched to galaxies typically contain at least 200 particles to minimise the potential bias induced by matching poorly-resolved haloes to the faintest galaxies (see also Sec. 5.3). Haloes and subhaloes are identified using ROCKSTAR halo finder (Behroozi et al. 2013a) and the CONSISTENT TREES merger tree builder (Behroozi et al. 2013b). Halo virial masses are calculated as regions with overdensity $\Delta_{\text{vir}} = 178$, following Bryan & Norman (1998). DarkSky assumes a flat Λ CDM cosmology with $H_0 = 68.8 \text{ km s}^{-1} \text{ Mpc}^{-1}$, $\Omega_m = 0.295$, scalar spectral index $n_s = 0.968$, and root-mean-square matter fluctuation on 8 Mpc/ h scales $\sigma_8 = 0.834$.

3 METHODOLOGY

3.1 Subhalo abundance matching

The fundamental assumption of SHAM is that there exists a near-monotonic relation between a galaxy property g (typically luminosity or stellar mass) and a halo property h (typically a function of virial mass and concentration):

$$N_{\text{gal}}(\bar{g}) = N_{\text{halo}}(\bar{h}), \quad (1)$$

where $N_{\text{gal}}(\bar{g})$ is the average number density of galaxies with $g > \bar{g}$ and $N_{\text{halo}}(\bar{h})$ is the average number density of haloes with $h > \bar{h}$. h is referred to as the *halo proxy* for g .

We present a new SHAM model that uses a continuous parameter to describe the halo proxy, interpolating between the peak halo virial mass and present-day virial mass. This is a modification of the proxy introduced in Lehmann et al. (2017), which interpolates between the halo virial mass and maximum circular velocity at the time of the peak halo mass.

The model has two free parameters, a generalised halo proxy m_α and a Gaussian scatter σ_{AM} . The halo proxy is defined to be an interpolation between the peak virial mass over the history of the halo, M_{peak} , and the present-day value M_0 :

$$m_\alpha = M_0 \left(\frac{M_{\text{peak}}}{M_0} \right)^\alpha. \quad (2)$$

m_α then provides a smooth, continuously varying dependence on the two halo properties as a function of α . If $\alpha = 0$ haloes are ranked simply by their present virial mass, and if $\alpha = 1$ by their peak virial mass. Ranking haloes by their peak virial mass ($\alpha = 1$) produces a stronger clustering signal than the present virial mass and increasing α further would further boost the clustering. It is a priori expected that ranking haloes by M_{peak} ought to be preferable to using M_0 (Conroy et al. 2006). Haloes with peak virial mass equal to their present-time virial mass are insensitive to α , so that tuning α directly controls the rank of haloes that have undergone mass stripping (typically subhaloes). For $\alpha > 0$ haloes that have peaked in mass in the past are ranked higher in the halo proxy list, whereas for $\alpha < 0$ such haloes are ranked lower. Therefore, α can be interpreted as controlling the fraction of simulated subhaloes

¹⁰ <https://darksky.slac.stanford.edu/>

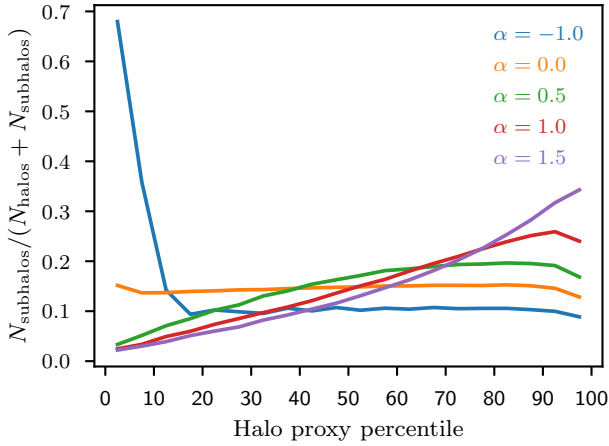


Figure 1. The proportion of subhaloes in the halo proxy list defined by Eq. (2) for different choices of α , percentile binned by the halo proxy ranking. When matching the haloes and subhaloes to galaxies, the most massive galaxy is assigned to the top-ranked halo, and so on down the list. Choosing $\alpha > 0$ boosts the proportion of upper-ranked subhaloes which are then matched to galaxies.

matched to galaxies. We demonstrate this in Fig. 1, which shows the dependence of the subhalo fraction on α in percentile bins.

The scatter in SHAM, parametrised by σ_{AM} , arises because the baryon content of a halo depends on parameters other than its mass, with the majority of scatter deriving from the halo mass accretion history (Tinker et al. 2017). We implement the scatter using the deconvolution method described in Behroozi et al. (2010), and treat it as a free parameter. For $\sigma_{AM} = 0$, abundance matching produces a one-to-one relation between the galaxy and halo proxy satisfying Eq. (1). If $\sigma_{AM} \neq 0$, then the galaxies matched initially at $\sigma_{AM} = 0$ are up- or down-scattered on the discrete galaxy-halo ladder. Non-zero values of σ_{AM} therefore add scatter to the galaxy-halo connection without affecting either the galaxy or halo proxy number densities themselves. It should be noted that our SHAM model does not explicitly account for the uncertainties in the measured g values (luminosity of mass), so that σ_{AM} contains both intrinsic and observational contributions.

We will also consider the possibility that the galaxies in our sample form in some subset of the total halo population. This is particularly relevant to HI-selected samples, which have overall significantly lower clustering than optically-selected samples (Guo et al. 2017; Papastergis et al. 2013). In particular, we consider pre-selection according to halo formation time, retaining only the haloes in the simulation with a peak-mass redshift lower than some cut-off z_{cut} , while ranking the remaining haloes by their present mass.

3.2 The galaxy luminosity and mass functions

Subhalo abundance matching requires as input the abundance functions of g in the observational data and h in the simulation. To calculate the luminosity and stellar mass functions for the optically selected samples we use the $1/V_{max}$ method (Schmidt 1968). This is a simple, non-parametric technique correcting for Malmquist bias, whereby intrinsically brighter galaxies are detected to larger distances. In this method, each galaxy is weighted by V_{max} , the maximum comoving volume in which it could be located and still be detected by the survey, given its intrinsic brightness and the

survey’s limiting apparent magnitude threshold (Malmquist 1920, 1922). Following the standard definition of apparent magnitude, the maximum redshift z_{max} at which i -th galaxy of absolute magnitude M_i can be located is calculated by solving the equation:

$$m_{lim} = M_i + 25 + 5 \log D_L(z_{max}) + K_i(z_{max}), \quad (3)$$

where m_{lim} is the limiting apparent magnitude of the survey and $D_L(z_{max})$ is the luminosity distance corresponding to z_{max} (Hogg 1999). $K_i(z_{max})$ is the estimated K-correction coefficient of the i -th galaxy if it were located at z_{max} . We fit a simple multi-layer perceptron algorithm (see e.g. Bishop (1995)) to predict the K-correction coefficient from the galaxy redshift, mass-to-light ratio, metallicity, and stellar formation rate such that $K_i(z_{max})$ is the network’s output when the observed galaxy redshift is replaced with z_{max} . A multi-layer perceptron consists of input and output layers of neurons, with possibly several intermediate hidden layers. The input layer contains one neuron per input feature and the output layer consists of a single neuron, producing a scalar output. The number of neurons and hidden layers is adjustable. Each neuron in the hidden layers and output layer is passed a transformed weighted sum of all outputs from the previous layer. By adjusting the weights the network learns the mapping from a set of features to a scalar. In this particular problem, the network shows little sensitivity to the number of hidden layers and we choose 3 hidden layers containing 8, 4, and 2 neurons. We use the SCIKIT-LEARN¹¹ implementation of the perceptron network.

Eq. (3) can also be solved for z_{min} , the minimum redshift at which a galaxy would have been observed by the survey given a bright-end limit on apparent magnitude. As our optically-selected catalogues are ultimately volume-limited, values of z_{max} above the survey limiting redshift are set to the limiting redshift (Sec. 2.1).

With $D_c(z)$ the comoving distance as a function of cosmological redshift, the maximum possible comoving volume for each galaxy is simply calculated under the assumption of a flat Universe ($\Omega_k = 0$):

$$V_{max} = \frac{\Omega_S}{3} \left[D_c(z_{max})^3 - D_c(z_{min})^3 \right], \quad (4)$$

where Ω_S is the solid angle spanned by the survey. $\Omega_S = 7966 \text{ deg}^2$ for the NYU-VAGC and NSA large-scale structure samples. The luminosity function $\Phi(M_r)$ is then obtained as a sum over the $1/V_{max}$ contributions from the N galaxies falling within the j -th absolute magnitude bin of width dM_r :

$$\Phi_j dM_r = \sum_{i=1}^N \frac{1}{V_{max,i}}. \quad (5)$$

The stellar mass function $\Phi(\log M_*/M_\odot)$ is calculated analogously, using the same $1/V_{max}$ coefficients but instead binning the galaxies by $\log M_*/M_\odot$. To avoid biased estimates, each survey must be complete to the chosen magnitude limit and contain no notably under- or overdense regions. To test this we apply the V/V_{max} test by calculating the V/V_{max} ratio for each galaxy, where V is the volume given by the redshift at which the galaxy was actually detected (Schmidt 1968). If the survey is complete and the sources are uniformly distributed, then V/V_{max} should be uniformly distributed from 0 to 1, which is true for both the NYU-VAGC and NSA samples.

¹¹ https://scikit-learn.org/stable/modules/neural_networks_supervised.html

The resulting LFs and SMFs for the optically-selected catalogues are shown in the first two panels of Fig. 2, where the residuals are taken with respect to the NYU-VAGC LF or SMF. In particular, both NYU-VAGC Petrosian and NSA elliptical Petrosian LFs and SMFs display similar number densities as expected. The NSA Sérsic LF and SMF are significantly different from the NYU-VAGC counterparts in predicting more galaxies at the bright end and fewer at the faint end. This is because the NSA photometric reduction includes more light in galaxies’ low surface brightness wings (Blanton et al. 2011).

We use ALFALFA HI masses (M_{HI}) and NSA elliptical Petrosian stellar masses to calculate the stellar, baryonic, and HI mass functions for our matched catalogue. The baryonic masses are estimated as

$$M_{\text{B}} = M_{*} + 1.4M_{\text{HI}}, \quad (6)$$

where the factor of 1.4 accounts for the presence of cosmic helium, as Big Bang nucleosynthesis produces $\sim 25\%$ of He by mass (Esmaeilzadeh et al. 1991). We calculate the effective volume V_{eff} for each galaxy in which it could have been located and still be observed by the survey following Zwaan et al. (2005). The V_{eff} s are the maximum-likelihood analogues of V_{max} values for optical-surveys, however calculated using the ALFALFA HI mass and velocity width completeness. As described in Sec. 2, we find that the matching process systematically eliminates nearby, low- M_{HI} galaxies. To account for this, we bin the galaxies in distance and HI mass, and calculate the proportion of galaxies in each bin with stellar mass estimates. We then multiply each galaxy’s V_{eff} value by fraction corresponding to the bin the galaxy is in. The resulting V_{eff} estimates are then used to calculate the differential mass functions according to Eq. (5).

In the third panel of Fig. 2 we show the resulting stellar mass function (SMF), baryonic mass function (BMF) and HI mass function (HIMF) for galaxies in the matched catalogue calculated using the V_{eff} values. The residuals are taken with respect to the matched catalogue’s SMF and for comparison we also show the NSA elliptical Petrosian SMF (optical selection). The HI-selected SMF drops off significantly faster than its optically-selected counterpart. On the other hand, the BMF is boosted relative to both the HI-selected SMF and HIMF and partially overlaps with the NSA elliptical Petrosian SMF. Compared to Jones et al. (2018) our HIMF (and consequently BMF) begins to turn over at the faint end: we discuss this in Sec. 5.3. In the matched catalogue there is a significant number of high baryonic mass galaxies that have non-negligible gas content, therefore explaining why the BMF number density is higher than SMF at the massive end of the mass function. The gas fractions are shown in Fig. 3.

3.3 Clustering measurements

To assess the extent to which the clustering of the SHAM mock catalogues resembles that of the real Universe we compute the projected two-point correlation function, w_p . This is defined as the integral of the full 3D galaxy correlation function ξ along the line of sight. Denoting separation along the line of sight π and perpendicular to the line of sight r_p , the projected two-point correlation function is calculated as

$$w_p(r_p) = 2 \int_0^{\pi_{\text{max}}} \xi(r_p, \pi) d\pi. \quad (7)$$

In theory, the upper integration limit should be $\pi_{\text{max}} \rightarrow \infty$ for $w_p(r_p)$ to be a purely real-space quantity. However, due to the finite size of the simulation or survey volume arbitrarily separated

pairs cannot be counted. Moreover, in practise distant pairs will show little correlation over the scales which we are interested in. Therefore, it is sufficient to pick some finite integration limit π_{max} , for which we choose 60 Mpc/h. This introduces a residual dependence on redshift-space distortions (RSD) when π_{max} is derived from redshift, and a further dependence on the RSD follows when the galaxy survey selection function is formulated in terms of redshift rather than true distance. Both of these conditions hold here. The effect of RSD is not large however Norberg et al. (2009), and we do not consider it further.

We calculate $\xi(r_p, \pi)$ using the Landy & Szalay estimator (Landy & Szalay 1993),

$$\xi(r_p, \pi) = \frac{\text{DD} - 2\text{DR} + \text{RR}}{\text{RR}}, \quad (8)$$

with DD, DR, and RR being the numbers of (possibly weighted) data-data, data-random and random-random pairs normalised by the total number of pairs. ξ is related to the excess probability of finding a galaxy pair separated by the redshift space distance $\sqrt{\pi^2 + r_p^2}$, relative to a uniform distribution of galaxies. The excess probability can be written as

$$dP = \bar{n}^2 [1 + \xi(r_p, \pi)] dV_1 dV_2, \quad (9)$$

where \bar{n} is the mean galaxy number density and $dV_{1,2}$ is the volume element associated with the two galaxies. For a uniform distribution $\xi = 0$, $\xi > 0$ indicates clustering of galaxies, and $\xi < 0$ means galaxies are less clustered than a uniform distribution.

When calculating ξ via Eq. (8) one of the required inputs is a distribution of uniformly distributed galaxies spanning the same volume as the observed galaxies. To ensure the same angular distribution, we use the NYU-VAGC large scale structure sample’s random catalogue, which also matches the NSA angular geometry. For the matched catalogue, we draw uniformly distributed samples on the sky from within the “mangle” polygons that define the survey geometry. Mangle is a software designed to deal with complex angular masks (Hamilton & Tegmark 2004). To each of these randomly-drawn points we assign the galaxy properties of interest (e.g. absolute magnitude and redshift) by randomly drawing samples from the survey, and then apply the desired absolute magnitude cut. This method has been verified for wide-angle surveys and avoids the need to explicitly model the surveys’ radial survival function (Ross et al. 2012), while providing a unified method for our optically-selected and HI-selected catalogues.

The uncertainty on the survey’s two-point projected space correlation function w_p is estimated via the jackknife resampling method (Norberg et al. 2009). We split the survey into 256 clusters in RA-dec by using the KMEANS-RADEC algorithm.¹² These clusters are calculated using the uniformly spaced random samples, to which the survey’s galaxies are then assigned. We calculate the correlation function, with the k -th cluster excluded, w_{pk} ; the jackknife covariance matrix is then calculated as

$$\mathbf{C}_{\text{jack}} = \frac{N-1}{N} \sum_{k=1}^N (w_{pk} - \hat{w}_p) (w_{pk} - \hat{w}_p)^{\text{T}} \quad (10)$$

where \hat{w}_p denotes the mean vector of all N jackknife estimates and N is the total number of clusters. We show the galaxy survey correlation functions for the NYU-VAGC and NSA catalogues in Fig. 4, where we bin the galaxies by M_r or $\log M_{*}/M_{\odot}$. Similarly, Fig. 5 displays the galaxy correlation functions for the matched

¹² https://github.com/esheldon/kmeans_radec

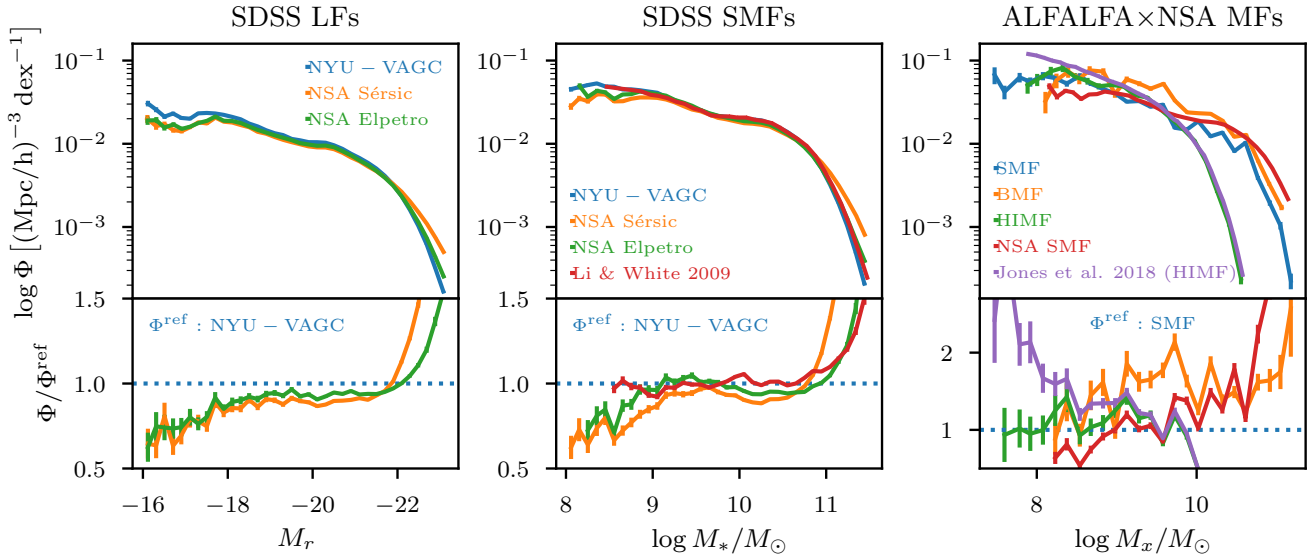


Figure 2. *Left:* r -band stellar luminosity functions for the NYU-VAGC Petrosian, NSA Sérsic and NSA elliptical Petrosian catalogues. *Centre:* stellar mass functions for the NYU-VAGC Petrosian, NSA Sérsic and NSA elliptical Petrosian catalogues along with the SMF from Li & White (2009) for comparison, which comes from a $z < 0.5$ NYU-VAGC sample. *Right:* stellar mass function, baryonic mass function and HI mass function for the ALFALFA \times NSA catalogue and comparison to NSA elliptical Petrosian SMF and the HI mass function (HIMF) of Jones et al. (2018), which is based on the full ALFALFA Spring sample. The subscript x indexes the mass definition and the error bars represent the standard Poisson counting error.

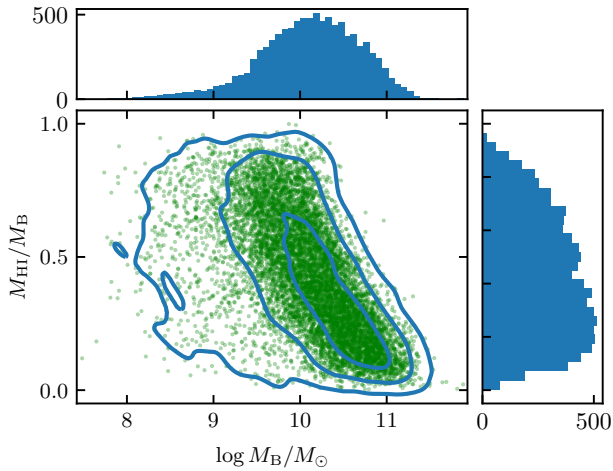


Figure 3. Gas fractions of galaxies in the ALFALFA \times NSA catalogue as a function of baryonic mass. The contours show the minimal areas enclosing 39%, 86% and 99% of the sample.

catalogue, where the galaxies are binned either by $\log M_B/M_\odot$, $\log M_{\text{HI}}/M_\odot$, $\log M_*/M_\odot$ or M_r .

We also estimate the uncertainty on the SHAM mocks’ two-point correlation function via jackknifing. However, as the simulated galaxies are distributed over a periodic box, here we leave out one sub-volume of size $25 \times 25 \times 400 \text{ Mpc}^3/h^3$ at a time. Furthermore, as we introduce scatter into the galaxy–halo relation through the SHAM parameter σ_{AM} , at each point in the SHAM parameter space we generate 50 independent mocks to estimate the “stochastic” contribution to the covariance matrix.

In Fig. 6 we show how varying the subhalo abundance matching parameters affects the two-point correlation function of the simulated catalogues (introduced in Sec. 3.3). In particular, one by one we vary α , σ_{AM} , and z_{cut} while keeping the other SHAM parameters fixed in the first three panels of Fig. 6. The residuals are always taken with respect to the first value in each panel’s legend. Increasing α gives stronger clustering on all scales as it results in preferentially ranking haloes with $M_{\text{peak}} > M_0$. Increasing the scatter σ_{AM} in the galaxy–halo connection decreases clustering across all scales as the up-scattered galaxies dominate over the down-scatter galaxies. However, it is possible that initially for small values of σ_{AM} the up-scattering dominates and boosts clustering on small scales. Lastly, introducing the z_{cut} threshold results in lowered clustering, as the earlier-forming haloes tend to cluster more strongly.

3.4 Likelihood Framework

We split each catalogue into several lower and upper-limited bins. By using bins with no objects in common, as opposed to thresholds as is more common, we minimise covariance between subsamples when combining their separate posteriors below. We use uniform priors and define a Gaussian likelihood over the SHAM two-point projected correlation functions, centred at the survey correlation function. The covariance matrix is taken to be the sum of the survey jackknife covariance, the SHAM jackknife and the SHAM covariance matrices. Therefore, the likelihood of the correlation function calculated from the SHAM simulation $\mathbf{x} = \mathbf{w}_p^{\text{AM}}(\boldsymbol{\theta})$ as a function of the model parameters (typically α and σ_{AM}) is

$$p(\text{D} | \boldsymbol{\theta}) = \frac{1}{\sqrt{|2\pi\boldsymbol{\Sigma}|}} \exp\left[-\frac{1}{2}(\mathbf{x} - \boldsymbol{\mu})^\top \boldsymbol{\Sigma}^{-1}(\mathbf{x} - \boldsymbol{\mu})\right], \quad (11)$$

where $\boldsymbol{\Sigma}$ is the aforementioned sum of covariance matrices, $\boldsymbol{\mu}$ is the survey correlation function, and k is the number of r_p bins.

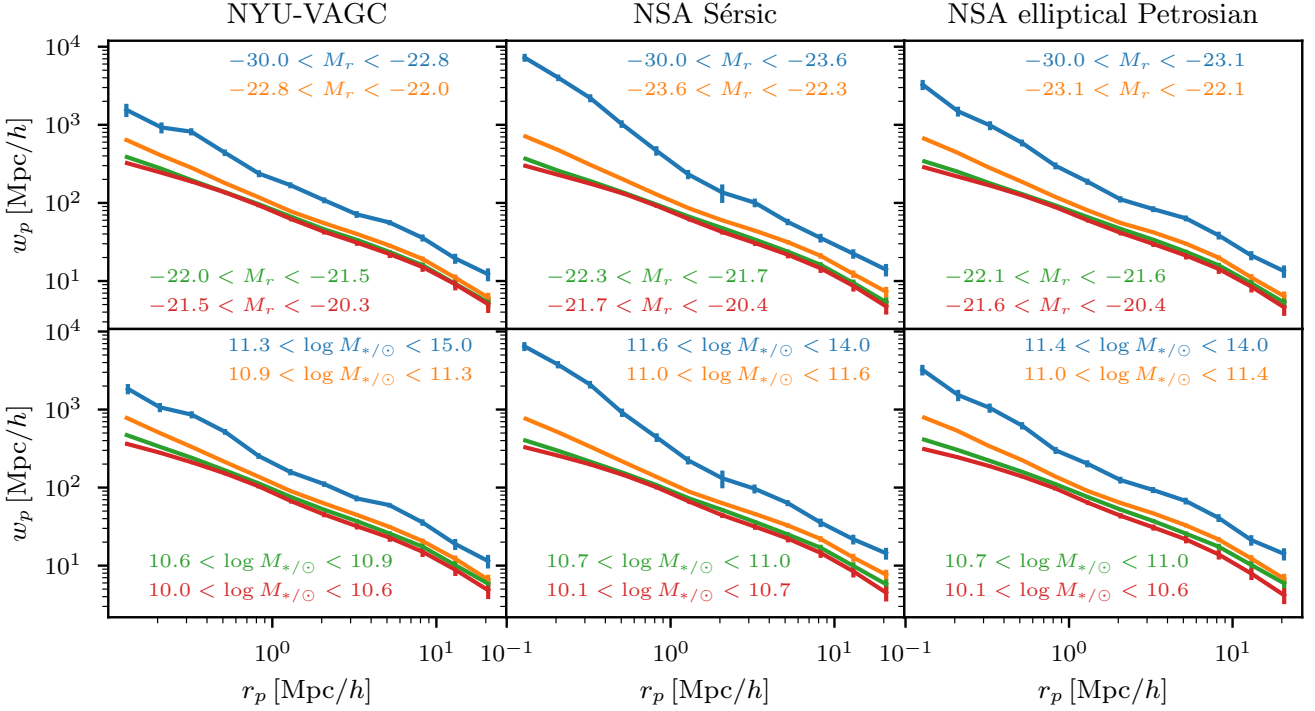


Figure 4. Two-point projected correlation function w_p for NYU-VAGC Petrosian, NSA Sérsic and NSA elliptical Petrosian photometries. Subsamples in the top row are defined by r -band luminosity while those in the bottom row are defined by stellar mass. These are the correlation functions used to calibrate our SHAM models. In particular, the small-scale two-point correlation function is sensitive to the presence of satellite galaxies which boost the clustering. The percentile selection used to determine the cuts in target quantities is given in Table 1. In what follows, the brightest (most massive) cut will be referred to as “1st subsample”, the next cut as “2nd subsample” and so on. We denote M_*/M_\odot by $M_{*/\odot}$.

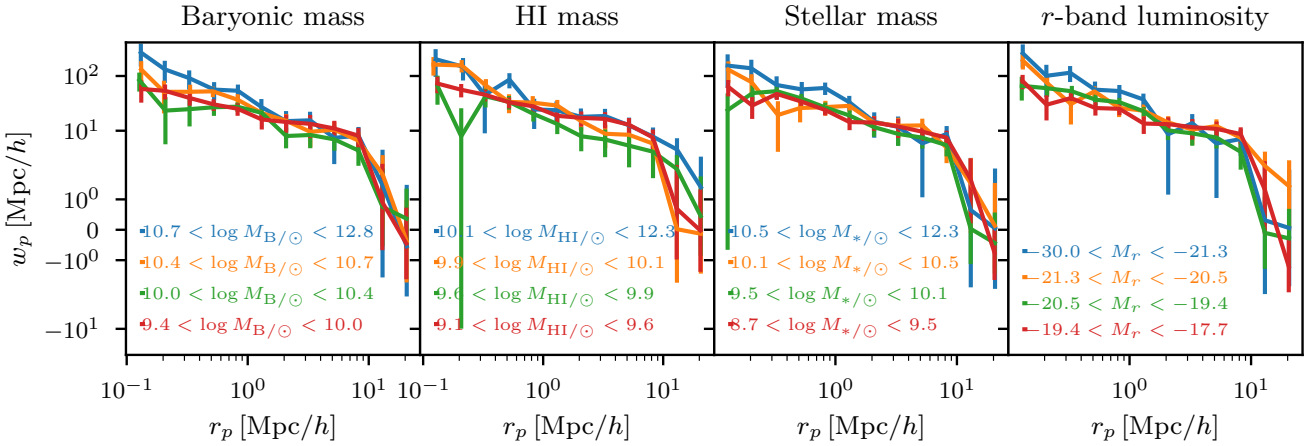


Figure 5. Two-point projected correlation function for the ALFALFA \times NSA catalogue. The panels are distinguished by the galaxy property used to define the subsamples. The percentile selection used to determine the cuts in target quantities is given in Table 5. We define $M_{x/\odot} \equiv M_x/M_\odot$, where M_x is either the baryonic, HI, or stellar mass.

We compare the goodness-of-fit of SHAM in various cases by means of the Bayesian evidence. For a single catalogue, with θ_i and D_i the fitted parameters and data in the i -th bin respectively, the evidence is given by

$$p(D_i | I) = \int p(D_i | \theta_i, I) p(\theta_i | I) d^n \theta, \quad (12)$$

where I denotes the model under consideration, which in our case reflects the choice of galaxy and halo proxy in SHAM, and the photometry and selection criteria of the sample. $p(D_i | \theta_i, I)$ is the likelihood of the data for given model parameters, while $p(\theta_i | I)$ is the prior on the parameters. To quantify parameter tension between bins we can compare the evidence of a model in which all bins share

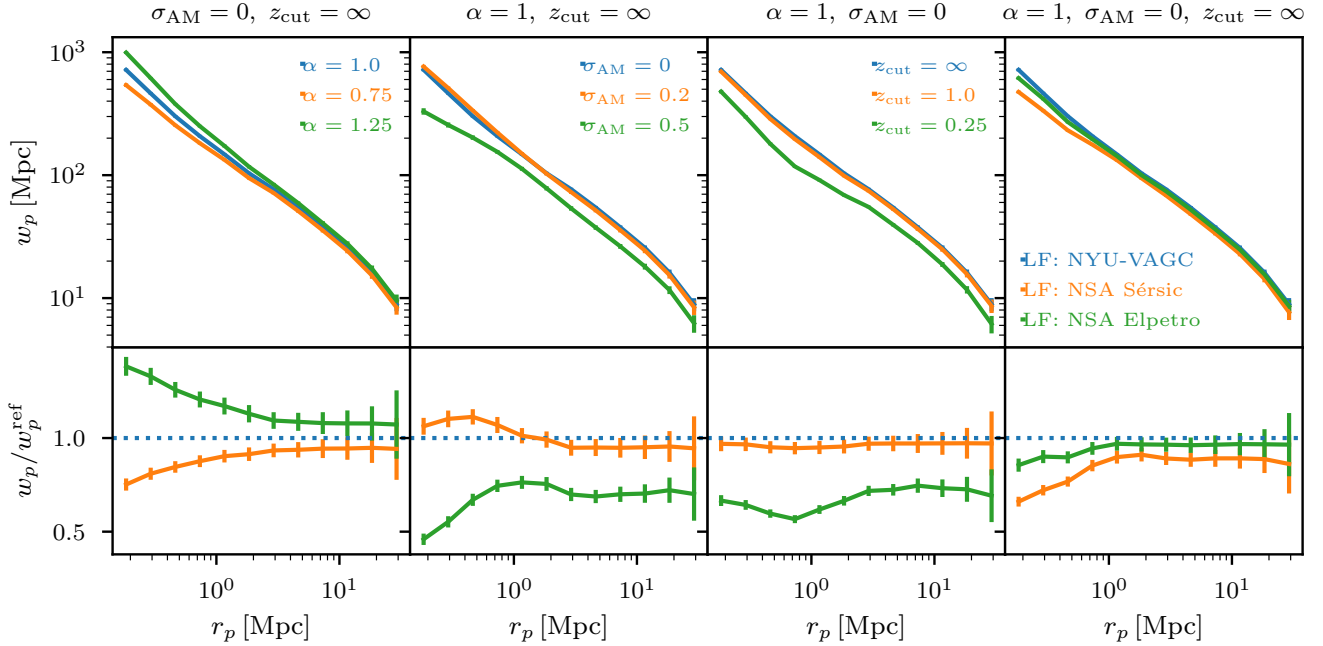


Figure 6. Variation of the simulated projected two-point correlation function w_p for NYU-VAGC LF-based SHAM with the model parameters α , σ_{AM} , and z_{cut} (see Sec. 3.1). The fourth panel shows w_p at a fixed posterior point but varying the input LF. The panel titles indicate the parameters that are kept fixed.

the same parameters to one in which the parameters are unique to each bin:

$$\mathcal{B}_{\text{tension}} = \frac{\int \left[\prod_i p(D_i | \theta, I) \right] p(\theta | I) d^n \theta}{\prod_i \left[\int p(D_i | \theta_i, I) p(\theta_i | I) d^n \theta_i \right]}, \quad (13)$$

where the product over i covers the bins that we wish to compare (Marshall et al. 2006). This yields the Bayes factor quantifying whether all bins share the same posterior parameters θ , or if each bin is better described by different parameters θ_i . This will allow us to answer the question of whether there is evidence for the running of SHAM parameters as a function of galaxy mass or luminosity.

Similarly, we can ask whether SHAM is more accurate when performed with luminosity M_r or stellar mass M_* . The Bayes factor for this comparison is

$$\mathcal{B}_{\text{proxy}} = \frac{p(D | I = M_r)}{p(D | I = M_*)}. \quad (14)$$

Here we can either compare evidences for specific bins, or we can combine the constraints from several bins before evaluating Eq. 14. For the latter, the combined evidence can either be calculated as in the numerator or denominator of Eq. (13), according to whether or not we assume the SHAM parameters are common between the bins. Lastly, we also calculate which photometric reduction pipeline is best-suited for SHAM, which is analogous to Eq. (14) but where the model instead corresponds to NYU-VAGC, NSA Sérsic, or NSA elliptical Petrosian photometry.

4 RESULTS

4.1 Optically-selected samples

We constrain the SHAM parameters α and σ_{AM} (Eq. 2) by comparing the two-point projected correlation function from the SHAM

mocks to that of the observational data. As described above, by splitting each catalogue into subsamples defined by lower and upper thresholds of luminosity or mass we can address whether the halo proxy shows any dependence on these quantities, which of them is best-suited for SHAM, and how the best-fit parameters respond to the photometric reduction.

After applying the cuts described in Sec. 2.1, we calculate the LFs and SMFs (Fig. 2) from the remaining galaxies, and the two-point projected correlation function for each catalogue subsample. The 1st subsample is assigned the brightest (or most massive) 1.5% of galaxies, the 2nd subsample is assigned the next 13.5%, the 3rd is assigned the next 25%, and finally the 4th bin is assigned the next 40% of galaxies. The faintest 20% of the galaxies in each catalogue are excluded, since they may be incomplete and/or the corresponding simulated haloes may not be well-resolved. This binning scheme allows for a selection of a comparable number of galaxies in each subsample despite the different SDSS photometric reductions used, and the same number of objects when comparing M_r to M_* . The samples do not share any objects, minimising their cross-correlation and statistical dependence. The binning is summarised in Table 1 for all optically-selected samples that we consider (NYU-VAGC Petrosian, NSA Sérsic, and NSA elliptical Petrosian). In what follows we will refer to the brightest (or most massive) subsample as the “1st subsample”, second brightest as “2nd subsample”, third brightest as “3rd subsample” and faintest as “4th subsample”.

The posteriors on the SHAM parameters for each subsample are shown in Fig. 7, where the rows reflect the three samples. Typically both M_r and M_* display similar posterior shapes in the α - σ_{AM} plane with the degeneracy between α and σ_{AM} and the dependence of the maximum-likelihood parameters on M_r and M_* being clearly visible. Some degeneracy between α and σ_{AM} should be expected because both control the simulated galaxy clustering, as shown in Fig. 6. Increasing α boosts the fraction of subhaloes matched to our

Percentile range	NYU			NSA Sérsic			NSA Elpetro		
	N	M_r	$\log M_*/M_\odot$	N	M_r	$\log M_*/M_\odot$	N	M_r	$\log M_*/M_\odot$
98.5% → 100%	8,040	(−30.0, −22.8)	(11.3, 15.0)	7,407	(−30, −23.6)	(11.6, 15.0)	7,090	(−30.0, −23.1)	(11.4, 15.0)
85.0% → 98.5%	72,353	(−22.8, −22.0)	(10.9, 11.3)	66,695	(−23.6, −22.3)	(11.0, 11.6)	63,810	(−23.1, −22.1)	(11.0, 11.4)
60.0% → 85.0%	133,988	(−22.0, −21.5)	(10.6, 10.9)	123,508	(−22.3, −21.7)	(10.7, 11.0)	118,166	(−22.1, −21.5)	(10.7, 11.0)
20.0% → 60.0%	214,381	(−21.5, −20.3)	(10.0, 10.6)	197,615	(−21.7, −20.4)	(10.1, 10.7)	189,065	(−21.5, −20.4)	(10.1, 10.7)

Table 1. Definition of the subsamples for the NYU-VAGC and NSA samples. The subsamples are split by M_r or M_* , with 100% corresponding to the brightest galaxy in the parent sample. The two-point projected correlation functions corresponding to these subsamples are shown in Fig. 4.

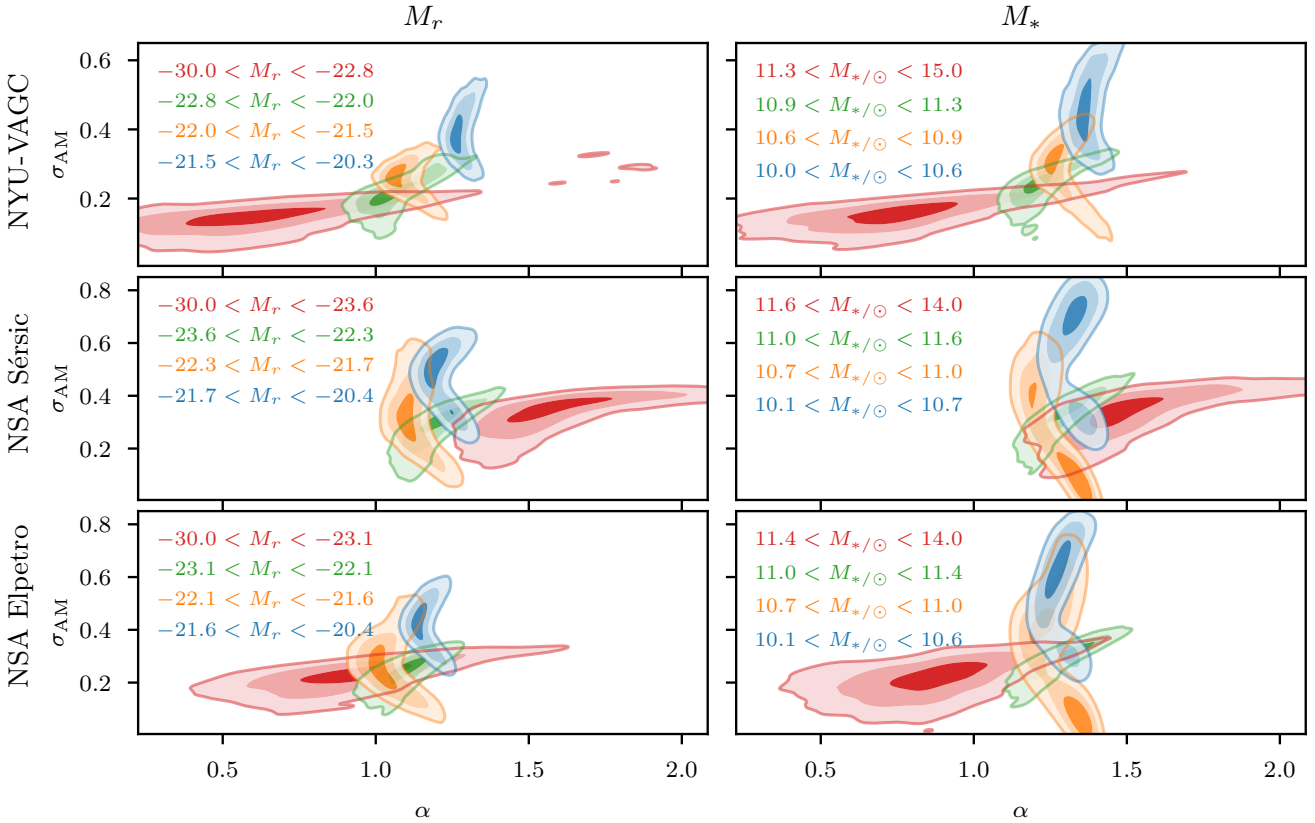


Figure 7. Posteriors on α and σ_{AM} for optically-selected samples. The contours show the minimal areas enclosing 39%, 86% and 99% of the sample. The rows distinguish different catalogues, while columns correspond to M_r and M_* . Each panel shows the posteriors for each of the four subsamples, from brightest in red to faintest in blue.

galaxies (Fig. 1), and consequently increases the small-scale clustering. On the other hand, increasing σ_{AM} weakens the clustering signal. In each sample we typically find that the fainter (or less massive) subsamples prefer larger values of σ_{AM} , and that M_* -based SHAM requires larger α and σ_{AM} than the M_r -based model. For a direct comparison of the samples, we show Fig. 8 where the individual plots display the comparison of SHAM model parameters between NYU-VAGC and NSA catalogues. We find that all catalogues show a similar SHAM parameter dependence in the 2nd and 3rd subsample. In the 4th (faintest) subsample a marginal difference between NYU-VAGC and NSA catalogues is visible, with the NYU-VAGC subsamples preferring larger values of α . However, most notably, in the 1st subsample (brightest and most massive) NSA Sérsic shows substantially stronger preference for larger values of alpha than the two Petrosian photometries, and therefore for populating stripped haloes. The fainter subsamples show a distinct

“banana shaped” posterior, which follows from our use of lower and upper bounds to define the samples. At relatively low values of σ_{AM} , the down-scattering of massive haloes can actually boost clustering, although for higher scatter values the up-scattering of less massive haloes dominates and lowers the clustering.

To answer the question of whether the SHAM galaxy–halo connection model shows systematic variation with galaxy brightness or mass, we analyse the individual posteriors following the formalism of Sec. 3.4 by comparing the models’ evidences. The Bayes factors are summarised in Table 2. We quote the tensions \mathcal{B}_{12} , \mathcal{B}_{23} , \mathcal{B}_{34} , \mathcal{B}_{14} , \mathcal{B}_{123} , and \mathcal{B}_{1234} , where the subscript ij gives the tension between i -th and j -th bin. No statistically significant evidence for either luminosity or stellar mass dependence is observed over the three brightest or most massive subsamples in either photometry sample. However, the NYU-VAGC Petrosian sample shows a strong tension between the 1st and 4th subsample in both

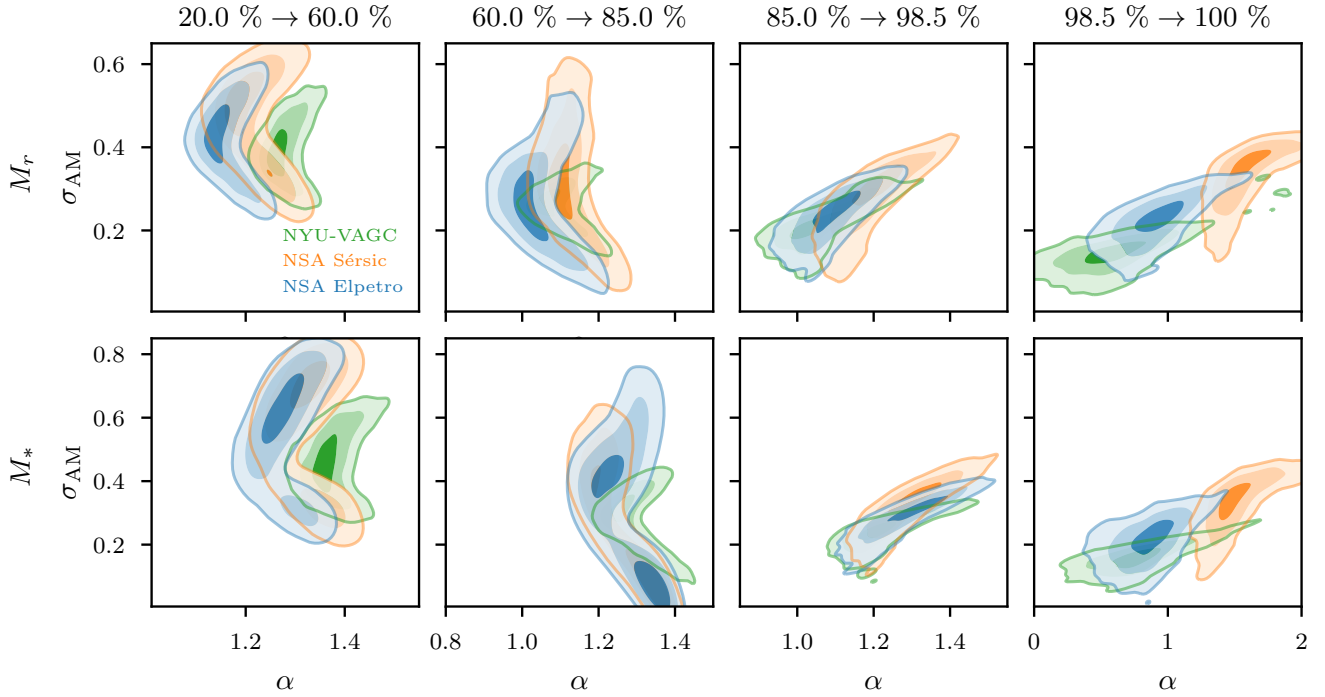


Figure 8. Direct comparison of posteriors on α and σ_{AM} (39%, 86% and 99% levels) between the NYU-VAGC Petrosian, NSA Sérsic and NSA elliptical Petrosian samples. Rows distinguish M_r vs M_* -based SHAM while columns distinguish the subsamples. Each subsample contains galaxies between the two percentile ranges indicated in the title, where 100% corresponds to the brightest or most massive galaxy. The subsamples are defined in Table 1.

M_r and M_* . Weaker tension is also observed in the other samples, indicating that the variation in the SHAM parameters occurs over a larger range of brightness and mass for NSA Sérsic and elliptical Petrosian samples. Consequently, we conclude that all four subsamples are mutually incompatible in all samples (and in both M_r and M_*) under the assumption of universal SHAM parameters, a result usually driven by the faintest subsample. As there is no statistically significant luminosity or stellar-mass dependence over the first three subsamples (except for the NSA Sérsic M_r sample), we quote the 90% confidence intervals on α and σ_{AM} in Table 3. As an example, the best two-point projected correlation function fits for the NSA elliptical Petrosian luminosity sample, along with the combined posterior fit, are shown in Fig. 9. We summarise how the best-fit values of α and σ_{AM} (and their 90% confidence intervals) depend on the subsample index – which can be viewed as a discrete sampling in M_r or M_* – in Fig. 10.

We can also compare the goodness-of-fit between M_r - and M_* -based SHAM models. First, we compare the evidences from the individual subsamples, as shown in the first four columns of Table 4. We find a weak preference for the luminosity-based model in each case. Next, if we assume that the halo proxy is specific to each subsample (“local” subscript in Table 4), this yields strong preference for the luminosity-based model in each sample. Lastly, we can also combine the evidence from the first three subsamples (found not to be mutually exclusive) assuming the halo proxy not to vary across the subsamples (“global” subscript in Table 4), producing again strong evidence in favour of M_r in the two Petrosian samples and inconclusive evidence in case of the NSA Sérsic sample. We therefore conclude that for Petrosian photometry, luminosity-based SHAM reconstructs observed the clustering significantly better than

	\mathcal{B}_{12}	\mathcal{B}_{23}	\mathcal{B}_{34}	\mathcal{B}_{14}	\mathcal{B}_{123}	\mathcal{B}_{1234}
NYU-VAGC M_r	3.2	17	0.029	2.1×10^{-5}	3.7	9.4×10^{-11}
NYU-VAGC M_*	2.6	18	3.5	8.0×10^{-5}	0.60	1.4×10^{-11}
NSA Sérsic M_r	0.060	5.0	0.74	0.10	0.028	4.2×10^{-5}
NSA Sérsic M_*	2.4	1.7	0.33	1.2	1.09	1.6×10^{-3}
NSA Elpetro M_r	10	14	0.67	0.59	190	5.6×10^{-6}
NSA Elpetro M_*	0.50	0.39	3.2	0.050	0.23	2.4×10^{-3}

Table 2. Bayes factors \mathcal{B}_i quantifying the consistency between α and σ_{AM} among various bin combinations i . $\mathcal{B} > 1$ indicate no tension, i.e. no evidence for dependence on M_r or M_* , while $\mathcal{B} \ll 1$ indicates significant tension. Faint green is used to distinguish strong support ($20 \leq \mathcal{B}_i < 150$) for consistency, deep green denotes very strong support ($150 \leq \mathcal{B}$) for consistency, and correspondingly in shades of red for tension. We find that the faintest (4th) bin shows strong evidence for different SHAM parameters to the other subsamples.

	α	σ_{AM}/dex	Domain
NYU-VAGC M_r	$1.09^{+0.03}_{-0.03}$	$0.21^{+0.01}_{-0.01}$	$M_r < -21.5$
NYU-VAGC M_*	$1.25^{+0.03}_{-0.03}$	$0.24^{+0.02}_{-0.02}$	$M_* > 10^{10.6} M_\odot$
NSA Sérsic M_r	$1.15^{+0.03}_{-0.03}$	$0.24^{+0.05}_{-0.05}$	$M_r < -21.7$
NSA Sérsic M_*	$1.23^{+0.03}_{-0.03}$	$0.26^{+0.05}_{-0.05}$	$M_* > 10^{10.7} M_\odot$
NSA Elpetro M_r	$1.03^{+0.04}_{-0.04}$	$0.23^{+0.03}_{-0.03}$	$M_r < -21.5$
NSA Elpetro M_*	$1.20^{+0.03}_{-0.03}$	$0.27^{+0.03}_{-0.03}$	$M_* > 10^{10.7} M_\odot$

Table 3. Maximum-likelihood and 90% credible intervals of α and σ_{AM} from the first three bins in luminosity or stellar mass (see Table 1).

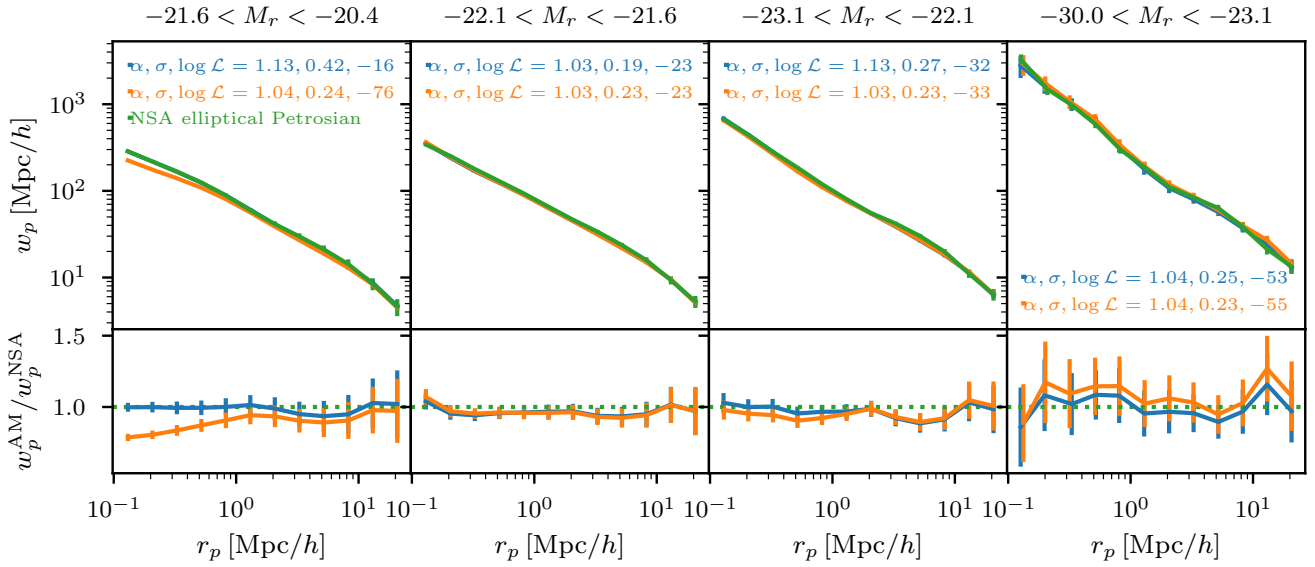


Figure 9. Comparison of each sample’s maximum-likelihood SHAM two-point projected correlation function and the maximum-likelihood combined constraint from the three brightest bins to the survey correlation function. Here we show the NSA elliptical Petrosian luminosity-based SHAM. $\log \mathcal{L}$ denotes maximum log-likelihood values and the residuals are taken with respect to the survey’s w_p .

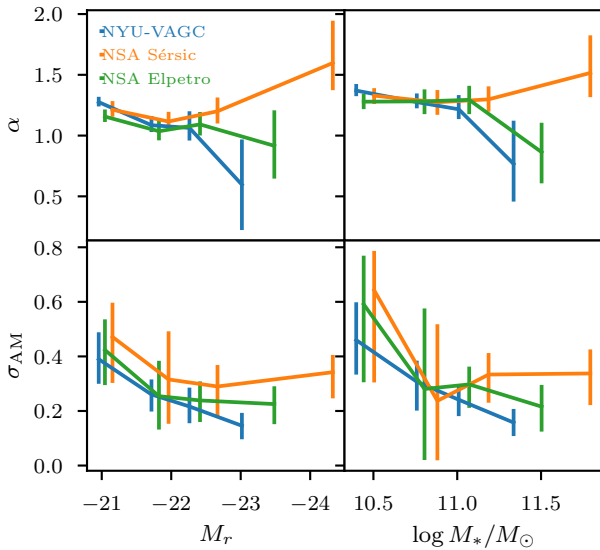


Figure 10. Best-fit SHAM parameters, and their 90% uncertainties, for our optically-selected samples as a function of M_r and M_* . The scatter in the galaxy–halo connection increases towards the faint end, while variation in the halo proxy is weak and sample-dependent.

stellar mass-based SHAM across the range of galaxy brightness that we consider.

Having explored each catalogue, we now address the question of which catalogue’s clustering can be best fitted with SHAM. In luminosity, considering only the first three, mutually consistent subsamples, we find the strongest preference for the NYU-VAGC Petrosian photometry, with strong support relative to NSA elliptical Petrosian photometry ($\mathcal{B} = 43 : 1$), and very strong support

	\mathcal{B}_1	\mathcal{B}_2	\mathcal{B}_3	\mathcal{B}_4	$\mathcal{B}_{123}^{\text{local}}$	$\mathcal{B}_{123}^{\text{global}}$	$\mathcal{B}_{1234}^{\text{local}}$
NYU	2.5	4.8	2.2	3.4	9.5	140	13
NSA Sérsic	0.64	16	7.9	2.4	81	1.7	190
NSA Elpetro	2.7	3.44	15	15	140	9.5×10^4	2200

Table 4. Bayes factors \mathcal{B}_i quantifying the preference for M_r over M_* -based SHAM in bin(s) i . $\mathcal{B} > 1$ indicates preference for the M_r -based sample. The “global” and “local” superscripts indicate whether we assume the halo proxy to be common to all subsamples (global), or peculiar to each subsample (local). The colours follow the convention of Table 2.

compared to NSA Sérsic ($\mathcal{B} = 5.3 \times 10^6 : 1$). The other possible comparison is across all four bins with luminosity dependence of the parameters: this yields again a very strong support for NYU-VAGC photometry relative to both NSA elliptical Petrosian ($\mathcal{B} = 190 : 1$) and Sérsic photometry ($\mathcal{B} = 6000 : 1$). We therefore conclude that the photometric reduction of NYU-VAGC – as has been used in most previous studies – is best suited for luminosity-based SHAM modelling.

The catalogues can also be compared for stellar mass-based SHAM. Over the first three, mutually consistent subsamples NYU-VAGC Petrosian photometry is strongly preferred over NSA elliptical Petrosian ($\mathcal{B} = 2.4 \times 10^4 : 1$) and Sérsic ($\mathcal{B} = 4.4 \times 10^4 : 1$) photometries. Finally, considering all four bins and assuming stellar mass dependence of the proxy yields again strong support for NYU-VAGC Petrosian photometry over NSA elliptical Petrosian ($\mathcal{B} = 4600 : 1$) and Sérsic photometry ($\mathcal{B} = 1.2 \times 10^4 : 1$). NYU-VAGC Petrosian stellar masses are therefore the best for use in SHAM.

4.2 HI-selected samples

For the HI-selected samples we use our ALFALFA \times NSA catalogue (see Sec. 2.1). We split the matched catalogue into 4 inde-

Percentile range	N	M_r	$\log M_*/M_\odot$	$\log M_B/M_\odot$	$\log M_{\text{HI}}/M_\odot$
87.5% \rightarrow 100%	1214	(-24.8, -21.3)	(10.5, 12.3)	(10.8, 12.3)	(10.1, 11.3)
67.5% \rightarrow 87.5%	1943	(-21.3, -20.5)	(10.1, 10.5)	(10.4, 10.8)	(9.9, 10.1)
40.0% \rightarrow 67.5%	2673	(-20.5, -19.4)	(9.5, 10.1)	(10.0, 10.4)	(9.6, 9.9)
10.0% \rightarrow 40.0%	2916	(-19.4, -17.7)	(8.7, 9.5)	(9.4, 10.0)	(9.1, 9.6)

Table 5. Definition of subsamples for the ALFALFA \times NSA catalogue.

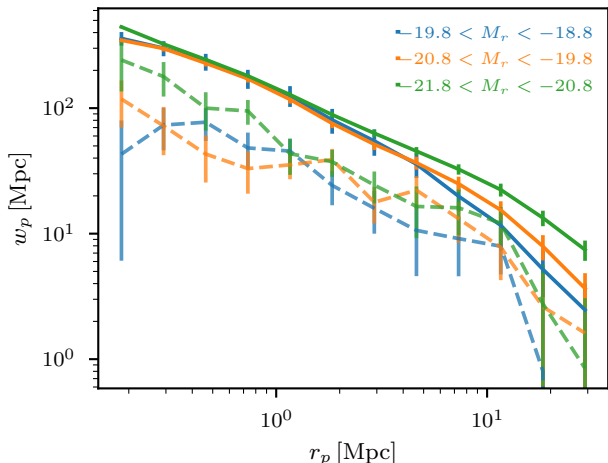


Figure 11. Comparison of optical (solid) vs HI-selected (dashed) two-point projected correlation functions in bins of luminosity from the NSA and ALFALFA \times NSA catalogues, respectively. Both the HI- and optically-selected samples use NSA elliptical Petrosian photometry, yet the former are significantly more weakly clustered.

pendent samples by stellar, HI or baryonic mass, or r -band absolute magnitude, as summarised in Table. 5. Because of the smaller survey volume compared to SDSS, the ALFALFA \times NSA catalogue contains significantly fewer massive galaxies. Therefore, to ensure that our subsamples are not noise dominated, we alter our binning scheme: the 1st subsample contains the top 12.5%, the 2nd subsample the next 20%, the 3rd subsample the next 27.5% and the final 4th subsample has the next 30% of galaxies. We calculate the projected correlation function (see Fig. 5) and luminosity and mass function (see Fig. 2) for each subsample following the formalism of Secs. 3.3 and 3.2.

Because of the HI-selection, the samples are substantially less clustered than the optically-selected ones. This is shown in Fig. 11, where we compare the clustering of the ALFALFA \times NSA catalogue to the NSA elliptical Petrosian sample for different subsamples in M_r (note that those subsamples are not the ones over which we perform SHAM and serve only for illustrative purposes here). By studying the matched catalogue we will be able to determine how optical vs HI selection affects the results of SHAM and whether SHAM can model clustering of HI-selected galaxies. We begin with our SHAM proxy of Eq. (2). As we will find that this model can only model HI clustering at very high σ_{AM} , we then proceed to modify the SHAM model to pre-select haloes with peak-mass redshift lower than z_{cut} , and then ranking haloes by present-day virial mass.

We show the posterior contours for baryonic, HI, stellar mass, and r -band luminosity-defined samples in Fig. 12. As the HI-selected samples are significantly less clustered, the posteriors show a noticeably different dependence on α and σ_{AM} . In each sample

(M_B , M_* , M_{HI} or M_r) we infer $\alpha < 0$, with the exception of the most massive subsample, with the posterior probability slowly decreasing towards the lower α limit we consider. This corresponds to preferentially occupying haloes with peak mass at present time, i.e. typically excluding subhaloes. At some negative threshold in α the model becomes dominated by haloes that peak at present time, and therefore stops being significantly affected by lowering α further. The exact threshold at which the clustering stops being significantly affected by varying α depends on the subsamples, although there is a systematic trend wherein the high-mass samples have this threshold at higher values of α . Therefore, we restrict the uniform prior to $-10 < \alpha < 1$. We do not need to go lower because the likelihood shows little dependence on α for large negative values.

We find substantial support for σ_{AM} of up to 2 dex. However, with such σ_{AM} the galaxy-halo connection introduced by the proxy is almost fully randomised, and hence the model contains little physical information. In fact, from the posteriors it is apparent that the ranking of the haloes becomes approximately randomised already at σ_{AM} of ~ 1 dex, which is when the posteriors become independent of σ_{AM} . At this point shuffling the haloes further has little effect on the predicted clustering. We therefore restrict the prior to $\sigma_{\text{AM}} < 2$ dex. This is typically observed at the higher range of allowed values of α , with the exception of the faint M_r and low M_* subsamples, which show strong support for zero scatter at large negative α . At such values of α the clustering has already been sufficiently reduced by the proxy, and therefore low σ_{AM} , which generally lowers clustering, is sufficient to match the observations.

We also show an example of the reconstructed correlation functions for the M_B sample in Fig. 13. These do not show as good agreement as the optical samples, which could be due to two main reasons. First, the proxy is not well-suited to HI-selected galaxies, which is exemplified by the fact that it prefers a very high SHAM scatter. Second, the ALFALFA \times NSA catalogue contains significantly fewer galaxies, and therefore its uncertainty on the two-point projected correlation function overwhelms the uncertainty from SHAM. This smears out the variation of the SHAM parameters. We note that the goodness of fit in the M_{HI} , M_* , or M_r subsamples is marginally worse than with M_B , although a significant conclusion cannot be drawn. We quote the maximum-likelihood points for each sample in Table. 6. We do not repeat the Bayes factor analysis for quantifying the tension between subsamples at fixed parameter values because our posteriors are significantly truncated by our prior ranges, which would bias the evidence.

Since in the previous cases the HI-clustering could only be reconstructed at the cost of either very high σ_{AM} or extreme values of α , we now introduce a parameter z_{cut} with the aim of reducing σ_{AM} . Ranking haloes by their present virial mass (i.e. fixing $\alpha = 0$), we pre-select only haloes with peak mass redshift lower than z_{cut} . For simplicity we consider only the baryonic mass sample. The resulting posteriors are shown in Fig. 14. The most massive subsample shows little dependence on z_{cut} , although the 2nd most massive clearly demonstrates that decreasing z_{cut} reduces σ_{AM} and the 3rd and 4th subsamples only allow $z_{\text{cut}} < 0.5$. The four subsamples' posteriors overlap, with a peak at $z_{\text{cut}} = 0.22^{+0.4}_{-0.2}$ and $\sigma_{\text{AM}} = 0.42^{+0.8}_{-0.2}$ dex

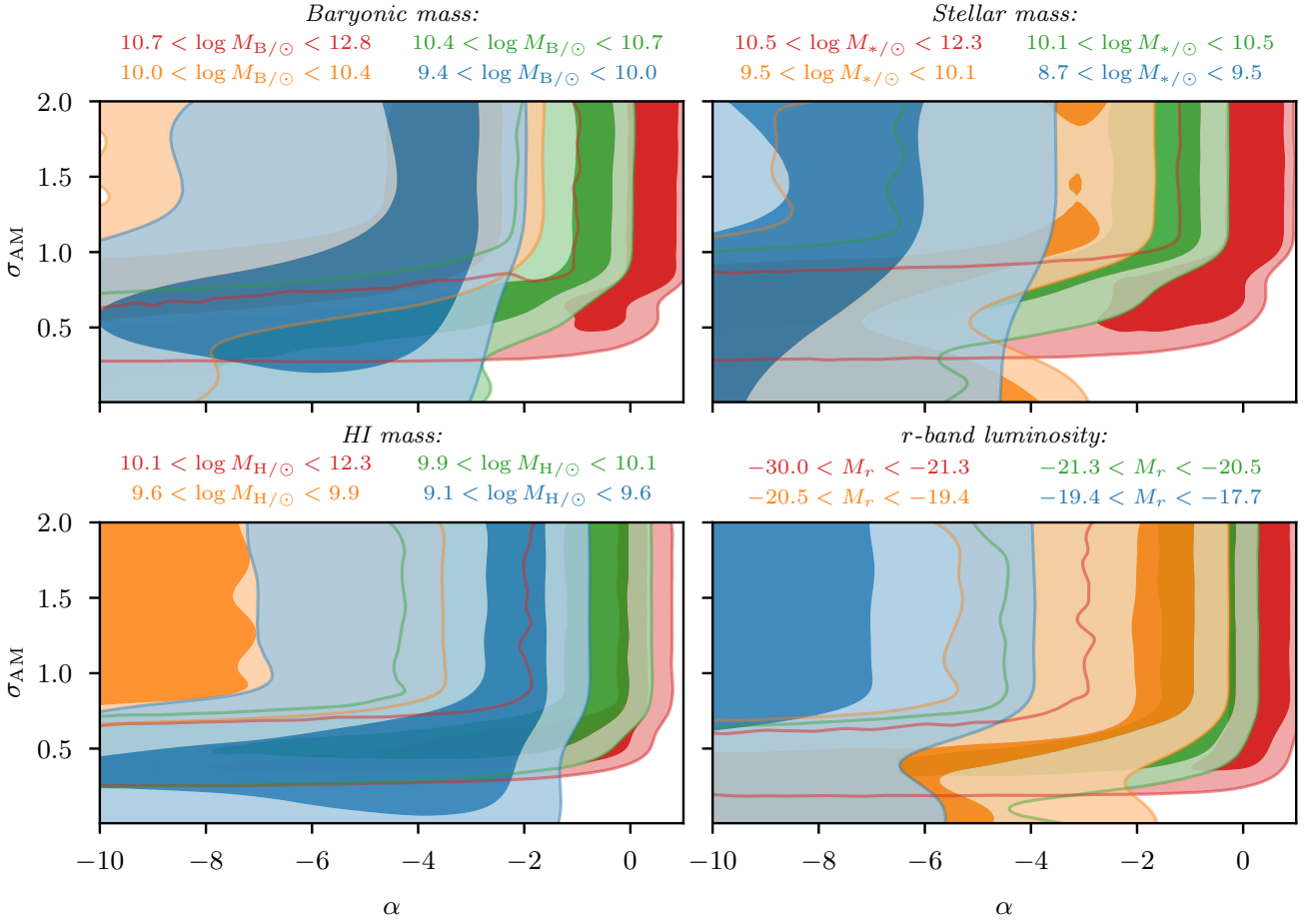


Figure 12. Posteriors on α and σ_{AM} for HI-selected samples from the ALFALFA \times NSA catalogue. The contours show the minimal areas enclosing 39% and 86% of the probability. The panels are distinguished by the galaxy property used in AM, as indicated.

Percentile range	$M_r : m_\alpha$			$M_* : m_\alpha$			$M_B : m_\alpha$			$M_{\text{HI}} : m_\alpha$			$M_B : z_{\text{cut}}$		
	α	$\sigma_{\text{AM}}/\text{dex}$	$\log \mathcal{L}$	α	$\sigma_{\text{AM}}/\text{dex}$	$\log \mathcal{L}$	α	σ_{AM}	$\log \mathcal{L}$	α	$\sigma_{\text{AM}}/\text{dex}$	$\log \mathcal{L}$	z_{cut}	$\sigma_{\text{AM}}/\text{dex}$	$\log \mathcal{L}$
87.5% \rightarrow 100%	0.50	1.5	-49	0.33	1.9	-47	0.59	2.0	-47	-0.89	0.56	-46	1.6	0.81	-46
67.5% \rightarrow 87.5%	-0.45	1.6	-43	-1.3	1.8	-43	-0.50	1.5	-40	-1.0	0.69	-45	0.13	0.22	-37
40.0% \rightarrow 67.5%	-9.8	0.0	-42	-9.1	0.0	-40	-7.8	0.76	-41	-10	0.90	-37	0.10	0.19	-38
10.0% \rightarrow 40.0%	-10	1.9	-37	-9.4	0.67	-37	-5.4	0.73	-35	-3.9	0.45	-37	0.32	0.72	-33

Table 6. Maximum-likelihood ($\log \mathcal{L}$) points with corresponding α (or z_{cut}) and σ_{AM} values for the ALFALFA \times NSA catalogue r -band luminosity, stellar mass, baryonic mass and HI mass-based SHAM models. m_α and z_{cut} in the headings distinguish our two SHAM models. The fits using z_{cut} have marginally higher maximum-likelihood values than using m_α .

(90% confidence intervals). This demonstrates that while ranking haloes by their present mass, σ_{AM} can be reduced by pre-selection on halo formation time (without z_{cut} we find $\sigma_{\text{AM}} = 0.83^{+0.6}_{-0.5}$ dex). Regarding the goodness-of-fit of the correlation function we only observe a marginal improvement when adding z_{cut} (see Table 6 for the maximum-likelihood points) because the uncertainty of the observed correlation function is significantly larger than that of the SHAM mocks.

5 DISCUSSION

5.1 Interpretation of the results

Our halo proxy is the product of the present virial mass times and ratio of peak-to-present virial mass to the power of α , thereby providing a simple model for halo assembly bias. The proxy reconstructs clustering of all the optically-selected samples we consider to high precision, and also works relatively well for HI-selected galaxies at the price of high scatter in the galaxy-halo connection.

By splitting the samples into lower- and upper-limited subsamples we were able to study the galaxy-halo connection as a function of luminosity and mass. We show that current data is sufficient to place meaningful constraints on this dependence for optically-

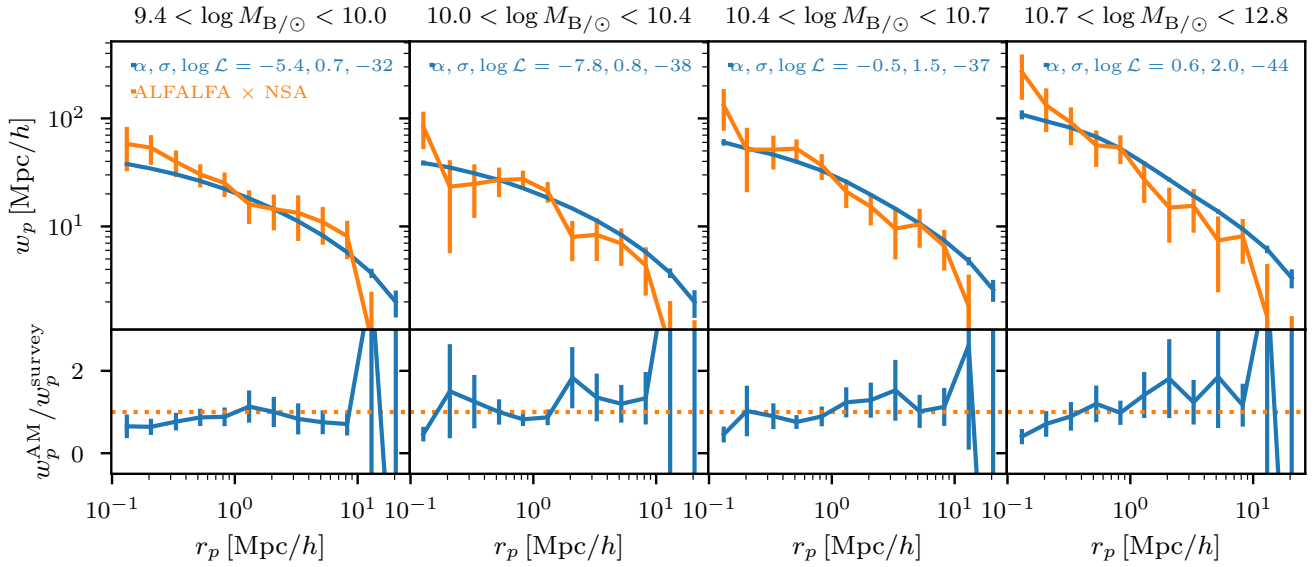


Figure 13. Comparison of the model two-point projected correlation functions for the ALFALFA \times NSA catalogue from baryonic mass-based SHAM vs that observed. The panels show different baryonic mass bins. $\log \mathcal{L}$ denotes the maximum log-likelihood values and the residuals are always taken with respect to the survey’s w_p .

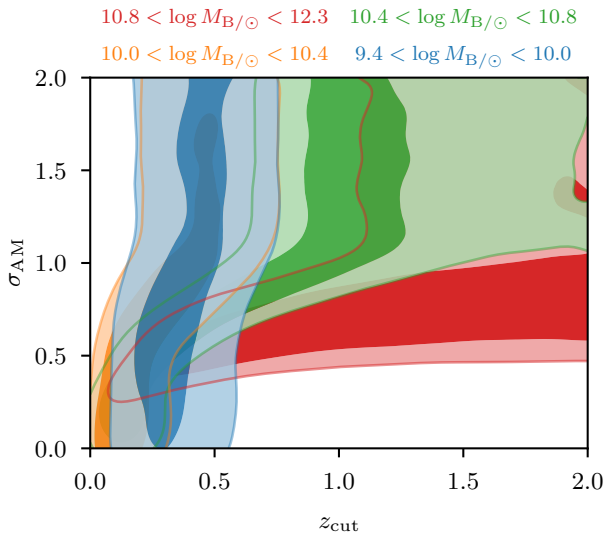


Figure 14. Posteriors on z_{cut} and σ_{AM} for HI-selected samples for baryonic mass-defined subsamples from the ALFALFA \times NSA catalogue. The posteriors overlap at $z_{\text{cut}} = 0.22^{+0.4}_{-0.2}$ and $\sigma_{\text{AM}} = 0.42^{+0.8}_{-0.2}$ dex (90% confidence intervals). The contours show the minimal area enclosing 39% and 86% of the probability.

selected galaxy samples, finding that fainter samples prefer higher α and, especially, σ_{AM} in the SHAM prescription. The hypothesis that the SHAM parameters are universal is strongly ruled out when comparing the faintest ($M_r > -21.5$ or $M_* < 10^{10.6} M_\odot$) and the brightest subsamples ($M_r < -22.8$ or $M_* > 10^{11.3} M_\odot$). In brighter subsamples ($M_r < -21.5$ or $M_* > 10^{10.6} M_\odot$) our model is consistent with $\alpha \approx 1.2$, corresponding to ranking haloes almost purely by the peak halo mass, and low σ_{AM} of ~ 0.25 dex suggesting that

secondary halo properties play only a minor role in the galaxy–halo connection. On the other hand, the galaxy–halo connection in the fainter subsamples is best fitted with higher α and with σ_{AM} of up to twice that for the brighter or higher-mass subsamples. This indicates that additional variables, not included in our model, are likely relevant in this regime.

We compare SHAM based on r -band luminosity to stellar mass and show that r -band luminosity is strongly favoured for SHAM under NYU-VAGC Petrosian photometry and NSA elliptical Petrosian photometry, while for NSA Sérsic the results are inconclusive. We also find that the SHAM scatter in the M_* model is typically larger. This is perhaps surprising given that the Tully–Fisher relation (TFR) is known to be tighter and more linear when expressed in terms of baryonic mass than luminosity (McGaugh et al. 2000), which would suggest that galaxy mass is a better indicator of halo properties than magnitude. However, the improvement in the baryonic Tully–Fisher relation (BTFR) is likely due primarily to the inclusion of gas in low-mass, gas-dominated spiral galaxies, and indeed there is little indication that the stellar mass TFR is tighter or more regular than the TFRs defined using luminosities in various bands (e.g. McGaugh 2005; McGaugh & Schombert 2015). It is likely that the increased σ_{AM} when using M_* indicates that the stellar masses themselves are imperfect, introducing scatter around the “true” M_* values.

We also investigate an HI-selected sample derived by cross-correlating the ALFALFA and SDSS data sets. We show that $\alpha > 0$ is strongly excluded in all but the most massive subsamples, which are only consistent with the observations for large $\sigma_{\text{AM}} \gtrsim 0.5$ dex. We find the galaxy mass or brightness (M_* , M_B , M_{HI} , M_r) of HI-selected galaxies not to correlate with the peak halo mass, and only weakly with the present-day virial mass in the most massive galaxy subsamples.

Decreasing α below 0, which corresponds to assigning bright galaxies preferentially to halos with masses peaking near the present day, typically reduces the scatter in the galaxy–halo connection. This suggests that to describe the galaxy–halo connection in HI galaxies

precisely it is necessary to incorporate other halo properties such as formation time or spin. These properties are far less important for optically-selected samples, where galaxy mass is strongly correlated almost exclusively with halo mass.

To investigate whether HI-selected galaxies are better associated with only a subset of the halo population we tried pre-selecting late-forming haloes before ranking them by their present virial mass. This has a similar effect to lowering α , so we do not consider models containing both parameters. We showed that by disregarding haloes that peaked at earlier times the scatter in the galaxy–halo connection can be significantly reduced, to values comparable to the scatter of the optical galaxy–halo connection. This suggests that HI-rich galaxies preferentially reside in halos that formed at lower redshift, which agrees with the conclusion of Guo et al. (2017).

In the optically-selected samples we find $\alpha \gtrsim 1$, which corresponds to ranking haloes by roughly their peak virial mass before matching them to galaxies. The best-fit values of α increase towards the fainter subsamples. Because increasing α (for $\alpha > 0$) boosts subhaloes, which in turn increases the fraction of satellites in the fainter subsamples, this reflects the fact that the SDSS galaxy sample contains fainter satellite galaxies as well. In sharp contrast, in the HI samples we find strong support for $\alpha < 0$. In this regime, stripped haloes are down-ranked (assigned to lower mass galaxies), so that the mock catalogues preferentially contain central haloes. This may reflect the fact that satellites are stripped of a large fraction of their HI gas, in agreement with the lower HI CF relative to the optical samples where the presence of satellites boosts the small-scale clustering.

In Fig. 15 we show the recovered $M_x - M_h$ relations using the best-fit SHAM parameters, where M_x represents optically-selected M_* from NYU-VAGC, HI-selected M_* from the ALFALFA \times NSA catalogue or M_B from the ALFALFA \times NSA catalogue. We observe that the HI-selection results in significantly lower M_* at fixed halo mass, especially below $10^{13} M_\odot$. To obtain these relations we have assumed that the SHAM parameters remain constant below the limits of our clustering constraints, despite the fact that we show earlier that these parameters do depend on galaxy brightness. We also extrapolate the mass and luminosity functions towards the faint end with power laws, on which the $M_x - M_h$ relation depends sensitively.

5.2 Comparison with the literature

Earlier studies of SHAM with SDSS galaxies found that values of scatter around 0.2 dex are appropriate for modelling the galaxy–halo connection in bright samples (Lehmann et al. 2017; Reddick et al. 2013). We find that the galaxy–halo connection is best fitted with scatter of ~ 0.25 dex in both M_r and M_* in the bright subsamples ($M_r < -22.8$ or $M_* > 10^{11.3} M_\odot$). In the faintest subsample scatter of ~ 0.5 dex was found necessary to fit the galaxy–halo connection. The precise boundaries of the faintest subsample considered depend on the specific catalogue, but typically covered the range of $-21.5 < M_r < -20.3$ or $10^{10.0} M_\odot < M_* < 10^{10.6} M_\odot$. Our analysis differs from Lehmann et al. (2017) in two main respects: 1) we use a different halo proxy, and 2) the subsamples over which we perform SHAM have no objects in common.

To investigate which of these differences is more significant we switch to the proxy of Lehmann et al. (2017), which interpolates between the halo virial mass and the maximum circular velocity evaluated at the peak halo mass. We find little difference in the results as the two proxies are strongly correlated. More significant is the effect of using binned vs thresholded subsamples. Previous

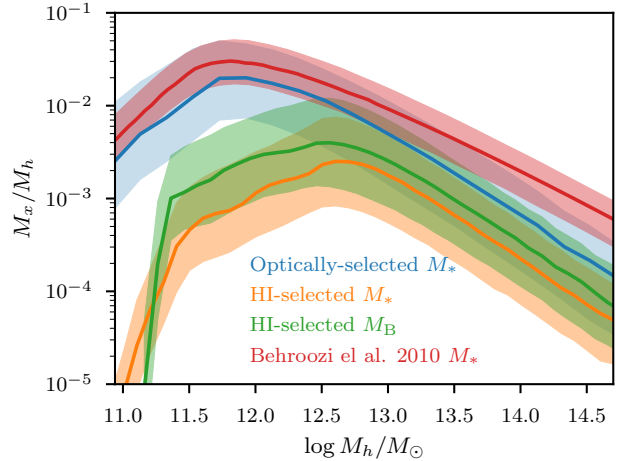


Figure 15. Relation of optically-selected M_* , HI-selected M_* and HI-selected M_B to present halo virial mass. The bands denote 1σ regions, and we compare to the $M_* - M_h$ relation of Behroozi et al. (2010).

works have typically used the latter, with the assumption that galaxies near the lower edge dominate the statistical properties of the sample. However, this assumption is only valid at the bright end where the luminosity or mass function declines sharply. Faint subsamples occupy the regime in which the luminosity function varies only slowly, making their statistical properties dependent on brighter galaxies as well. These subsamples cannot therefore be considered independent when deriving joint constraints on parameters of the galaxy–halo connection. We tested this by removing the upper limits on our subsamples, which resulted in notably different posteriors. In particular the fainter samples’ posteriors became skewed towards those of the brighter subsamples, i.e. towards lower scatter.

There have been few past studies of the galaxy–halo connection of HI-selected samples. Papastergis et al. (2013) studied the clustering of $\sim 6,000$ HI-selected galaxies from the 30% complete ALFALFA data set, finding no evidence for a dependence of clustering on HI mass. They argue from this that HI mass is not strongly correlated with halo mass, and that secondary halo properties such as spin therefore play an important role in the HI galaxy–halo connection. In contrast, Guo et al. (2017) found that clustering increases significantly at higher HI mass in $\sim 16,000$ HI-selected galaxies from the 70% complete ALFALFA data set, and that the galaxy–halo connection of these galaxies can be fitted reasonably well by an SHAM model that ranks haloes by the peak circular velocity. This required however a pre-selection of late-forming halos according to the parameter $z_{1/2}$, defined as the redshift at which a halo reaches half its peak mass. The $z_{1/2}$ threshold was found to decrease in higher HI mass subsamples.

We have not pursued here a detailed study of the clustering amplitude dependence on mass. Based on a simple qualitative comparison we note that the clustering of the ALFALFA \times NSA catalogue shows only marginal dependence on HI mass, although we find a stronger dependence on the baryonic mass. Similarly to Papastergis et al. (2013) and Guo et al. (2017) we find that using simply halo mass as the SHAM proxy cannot reproduce the observational data due to the poor correlation with the HI-selected galaxy mass, even considering the possibility of scatter in the relation. The proxy we define here, which incorporates information about the halo formation time alongside with the halo mass, can reproduce the clustering

reasonably well at the cost of a large scatter. Lastly, and similarly to Guo et al. (2017), we also try replacing the proxy by a pre-selection of late-forming haloes in the simulation before performing SHAM. This results in a marginally better goodness-of-fit than the peak-to-present halo mass proxy and, more importantly, reduces the SHAM scatter. We find that galaxies with $M_B \gtrsim 10^{10.5} M_\odot$ are insensitive to variations of z_{cut} , as most of the highest-mass halos peak in mass at $z = 0$, and that in lower-mass galaxies reducing the z_{cut} threshold decreases the SHAM scatter.

Having fitted our SHAM model, we also compare the predicted galaxy-to-halo mass relations to that of Behroozi et al. (2010) in Fig. 15. Compared to Behroozi et al. (2010), our relation predicts on average lower M_* at a given halo mass, although our model also predicts higher scatter in the relation due to larger σ_{AM} . If we fix $\sigma_{\text{AM}} = 0.2$ dex we obtain only small differences to Behroozi et al. (2010) due to our differing SHAM prescriptions.

5.3 Systematic uncertainties

The two observational inputs to SHAM are the halo catalogue from the N -body simulation and the galaxy luminosity or mass function. The precision of the simulation depends on the particular N -body code, simulation volume and initial conditions. Schneider et al. (2016) found that the standard N -body codes agree to within one percent at $k \leq 1 h\text{Mpc}^{-1}$, the regime of relevance here. The ROCKSTAR halo finder was tested in Knebe et al. (2011), showing excellent precision in comparison to other halo finders. Moreover, some of the low-mass haloes may not be well resolved or may have been stripped of sufficient mass to fall beneath the simulation resolution limit, potentially biasing the faintest or least massive subsamples we consider (Contreras et al. 2020). In our halo catalogue the minimum mass halo consists of ~ 40 particles, which is insufficient to be well-resolved (Diemer & Kravtsov 2015). Therefore, we chose a conservative lower threshold for the faintest subsamples, such that the majority of matched haloes lie well above the resolution limit. Even in the faintest subsamples, $> 95\%$ of haloes contain > 200 particles, with the median number being around 5000. To calculate the galaxy luminosity and mass functions for the optically-selected galaxies we used the $1/V_{\text{max}}$ method, which provides an unbiased, normalised estimate if the survey is complete and contains no significantly under- or over-dense regions (Efstathiou et al. 1988). We verified that this is true for our catalogues using the V/V_{max} test in Sec. 3.2. With the HI-selected galaxies we used an analogous non-parametric $1/V_{\text{eff}}$ approach (see Sec. 3.2).

The matching of ALFALFA to NSA systematically eliminated low gas mass, optically faint galaxies. Our method for correcting this is described in Sec. 3.2. Nevertheless, the fact that the HIMF in Fig. 2 begins to turn over at the faint end suggests that this bias correction was not entirely successful. Thus, the ALFALFA results are less reliable at low than high mass, although fully correcting for the exclusion of optically faint galaxies would not alter our qualitative conclusion that regular SHAM performs poorly on HI-selected samples.

The survey two-point projected correlation function, used to constrain the SHAM parameters, requires as input a uniform distribution of random points matching the survey radial and angular selection criteria. For the radial distribution we used the ‘‘shuffled method’’ (see Sec. 3.3), which provides a less biased estimate than, for example, modelling the survey redshift distribution using a spline fit (Ross et al. 2012). On the other hand, we ignored the surveys’ angular selection. In NYU-VAGC the angular selection can be estimated from the spectroscopic completeness of sectors,

which yields the proportion of objects with acquired spectra from each sector. We tested applying the NYU-VAGC angular selection corrections and found that it had a negligible effect on the scales we considered. Another possibility is to weight the galaxy pairs when calculating the correlation function, in order to weight areas with different number densities differently (e.g. Feldman et al. 1994). We found the inclusion of such weighting to have a little effect on our results. This is because the optically-selected NYU-VAGC and NSA catalogues contain no significantly under- or over-dense regions. On the other hand, due to the weak clustering of the HI-selected galaxies a precise modelling of the correlation function of the full ALFALFA sample should take such weighting into consideration. Our use of only a subset of the ALFALFA data that is highly complete (Sec. 2.1) means that a weighting scheme is not crucial.

We did not perform model selection on the HI-selected samples because our prior constraints eliminated parts of the posterior with potentially substantial probability density. The constraints on the prior were necessary because the peak-to-present halo mass proxy that we used is not well-suited for HI-selected galaxies, as can be seen from the large preferred scatter values and the fact that the posterior support does not dwindle significantly for very large or small values of α or scatter. More importantly, the large scatter necessitated extrapolation of the mass function at the faint end, which was not constrained by our data, thus potentially biasing the results. Lastly, a possible source of bias in the ALFALFA \times NSA catalogue is the matching of the HI to optical sources. This was done by enforcing an angular tolerance of $5''$ and a line-of-sight distance tolerance of 10 Mpc (Sec. 2.1), which will likely misclassify a small fraction of galaxies. As a qualitative check that this fraction is small, we find few if any obvious outliers in Fig. 3.

5.4 Future work

Most subhalo abundance matching works, including this one, have focused on the local Universe in which galaxy properties may be precisely measured. This has led to a good understanding of the galaxy–halo connection at $z = 0$ (Wechsler & Tinker 2018). In contrast, a detailed understanding of the galaxy–halo connection as a function of cosmic time is lacking. Therefore, an interesting question is whether our SHAM modelling holds at $z > 0$, and if so how its parameters evolve with redshift. This would allow for generating accurate mocks with SHAM for upcoming galaxy surveys which extend considerably beyond $z = 0$, e.g. Euclid and the Large Synoptic Survey Telescope (LSST) (Laureijs et al. 2011; Ivezić et al. 2019).

Ours is one of few studies to explore the HI galaxy–halo connection in statistical detail. In this and previous works it has been shown that halo assembly bias plays an important and non-trivial role for HI-selected galaxies, with hints that properties like halo formation time or spin are critical components of the galaxy–halo connection. A first step towards designing an SHAM model better suited to HI-selected samples would be to introduce a 2D halo proxy, which includes both a primary halo property (mass or velocity) and a secondary halo property like spin, formation time or concentration. We were unable to make strong claims here due to limitations of our proxy and the relatively low number of HI-selected galaxies in our sample, which leads to large uncertainty on the measured correlation function. Future HI surveys like those conducted by the Square Kilometre Array (SKA) (Dewdney et al. 2009) will significantly improve our understanding of this important but poorly-understood aspect of the galaxy–halo connection. In addition, precise inference of the HI–halo connection at the faint end will require the HIMF of

the matched catalogue to be accurately modelled down to low mass. One way to avoid the downturn that we observe in Fig. 2 – at the price of partially specifying the relation a priori – would be to force the HIMF to match the Schechter function fit to an HIMF derived from HI information only, for example Jones et al. (2018).

In terms of how the galaxy–halo connection changes with galaxy mass or brightness, there are two possible immediate extensions. The first would be to investigate the variation of the SHAM parameters even further into the faint end, for $M_r > -20.3$ or $M_* < 10^{10} M_\odot$. This would provide more definitive evidence for the brightness variation of those parameters and help pin down the precise form of this variation. The second would be to introduce a halo proxy that is explicitly luminosity- or mass- dependent. This would however require a substantial revision of the subhalo abundance matching formalism to introduce a coupling between the galaxy and halo parameters.

The galaxy–halo connection of faint galaxies (beyond the SDSS limiting magnitude at distances required for a statistical sample) remains largely unexplored in the context of subhalo abundance matching. The formation and properties of low-mass galaxies serve as important tests of the Λ CDM model (Bullock & Boylan-Kolchin 2017). We have shown that the faintest subsamples considered ($-21.5 < M_r < -20.3$) require substantially higher scatter in the galaxy–halo connection as well as an altered shape (higher proxy parameter α) compared to brighter samples. This suggests that to model the galaxy–halo connection of faint galaxies ($M_r > -19.6$) via SHAM a different set of assumptions may be needed, especially concerning satellite galaxies and the importance of halo properties beside virial mass. Our model predicts lower stellar masses at a given halo mass than those in the literature, and we show that the $M_* - M_h$ relation of HI-selected galaxies from the ALFALFA survey is substantially different at the faint end. Extrapolating further, this may help to resolve the missing satellites (Klypin et al. 1999; Moore et al. 1999) and Too Big To Fail (Boylan-Kolchin et al. 2012) problems.

It is also of interest to investigate the galaxy–halo connection as a function of galaxy type. For example, bluer, more gas-dominated galaxies from SDSS would be expected to be more similar to HI-selected galaxies. This could be explored by introducing subsamples defined by galaxy type and performing a similar analysis to the one we present here. Moreover, our finding of a significantly larger SHAM scatter for fainter samples suggests that assembly bias plays a more important role at the faint end. It would therefore be interesting to investigate whether the inclusion of other secondary halo properties into the galaxy–halo connection can reduce the scatter in this regime.

A good understanding of the galaxy–halo connection is also of use in constraining cosmological parameters from galaxy clustering. While on large scales a simple bias model between galaxy counts and the matter density is sufficient, on smaller scales the details of how galaxies populate halos becomes important. Current surveys typically neglect such scales (e.g. DES Collaboration et al. (2021); Pandey et al. (2021)), thereby discarding much pertinent information. The alternative is to use an empirical technique like SHAM to generate mock galaxy catalogues and then marginalise over the added parameters in constraining cosmology (e.g. Reddick et al. (2014)). Systematic effects in the empirical technique must be strictly under control for this approach to be viable.

Lastly, stronger constraints may be obtained by comparing to additional observational data. For example, application of a group finder would allow modelling of the conditional stellar mass functions of satellite and central galaxies (Reddick et al. 2013).

6 CONCLUSIONS

We have studied the galaxy–halo connection in both optically and HI-selected galaxies by means of the subhalo abundance matching (SHAM) technique. For the optically-selected galaxies we used the New York University Value Added Galaxy Catalog with Petrosian magnitudes and stellar masses as well as the Nasa Sloan Atlas galaxy catalogue with both the elliptical Petrosian and Sérsic photometry. We matched galaxies from the ALFALFA survey to the Nasa Sloan Atlas to obtain HI-selected galaxies with baryonic mass estimates. We introduced a new parametrised SHAM halo proxy which interpolates between the present and peak virial masses, thereby including a simple model for halo assembly bias. The SHAM parameters are constrained using measurements of the two-point projected correlation function in bins of luminosity or mass. We show our model to be well-suited to optically-selected galaxies but less so for HI-selected samples where it requires a large scatter, due to the significantly weaker clustering. This likely indicates that unmodelled halo and/or galaxy properties are important in the HI–halo connection. As one way to investigate this we tried pre-selecting only the latest-forming haloes to host HI-rich galaxies, and showed this to be successful in reducing the SHAM scatter. Our specific conclusions are as follows:

- The best-fit SHAM parameters of optically-selected galaxies are dependent on galaxy brightness and mass. Galaxies fainter than $M_r \approx -21.5$ or $M_* \approx 10^{10.6} M_\odot$ require an SHAM scatter up to twice as large as the brighter subsamples, as well as systematically larger values of the halo proxy α . The strong tension between the SHAM parameters in bright and faint subsamples can be seen in Figs. 7 and 10. The hypothesis of a universal halo proxy is valid only for $M_r \lesssim -21.5$ and $M_* \gtrsim 10^{10.6} M_\odot$, for which we quote the best-fit parameters in Table 3. In the HI-selected samples we also showed that the best-fit SHAM parameters depend on galaxy mass (Fig. 12 and Fig. 14), and in particular that lower-mass subsamples prefer lower values of α . This indicates that halos with mass peaking near the present day, i.e. central haloes, are preferentially populated. However, because our halo proxy is not ideal for such samples we were not able to study this dependence thoroughly (see Sec. 5.3).

- Different photometric pipelines give marginally different posteriors for the SHAM parameters (Fig. 8). This is most significant in the brightest ($M_r < -22.8$ or $M_* > 10^{11.3} M_\odot$) and faintest ($M_r > -21.5$ or $M_* < 10^{10.6} M_\odot$) subsamples. The two selection criteria – optical and HI – strongly affect the preferred SHAM parameters, producing mutually exclusive posteriors. Using our peak-to-present virial mass proxy we find that for optically-selected galaxies the proxy parameter is typically $\alpha \approx 1.2$ (Fig. 7), which corresponds to ranking haloes nearly by their peak mass. On the other hand, for HI-selected galaxies we infer $\alpha \leq 0$, with lower values preferred for fainter subsamples (Fig. 12). This indicates that halo assembly bias plays out very differently for HI- than optically-selected samples, and is likely more important. To investigate this, we considered a pre-selection of haloes by the peak mass redshift, retaining only haloes that formed before some threshold z_{cut} and ranking the remaining haloes by their present virial mass. The constraints when combining all subsamples are $z_{\text{cut}} = 0.22_{-0.2}^{+0.4}$ and $\sigma_{\text{AM}} = 0.42_{-0.2}^{+0.8}$ dex, the latter being a factor of two lower than when z_{cut} is not included.

- The NYU-VAGC Petrosian photometry pipeline maximises the goodness-of-fit of both the r -band luminosity and stellar mass-based SHAM. In both cases basing SHAM on NSA Sérsic photometry re-

covers the observed clustering worse than either of the two Petrosian photometries.

- In the optically-selected samples we compared the goodness-of-fit quality of r -band luminosity to stellar mass-based SHAM. The Bayes factors for the model comparisons are shown in Table 4. All the samples we consider prefer M_r -based SHAM, with Bayes factors of 13, 190, and 2200 for NYU-VAGC Petrosian photometry, NSA elliptical Petrosian and Sérsic photometries respectively. The preference for M_r -based over M_* -based SHAM likely stems from scatter around the “true” stellar masses introduced by the M_* definitions that we investigate. For the HI-selected galaxies we considered baryonic mass, HI mass, stellar and r -band luminosity SHAM; however, because our model has non-vanishing posterior probability at the prior boundaries in both α and scatter, we were not able to assess quantitatively which galaxy variable is best suited to use in SHAM in that case.

- The HI-selected samples are substantially less clustered than their optically-selected counterparts across the full range of scales we investigate, and the mass or brightness of HI-selected galaxies is a much poorer indicator of clustering (Fig. 11). The HI selection also reduces the stellar mass function at the bright end (Fig. 2). Despite the different mass function shape, the weaker clustering still results in substantially different values of the SHAM proxy and scatter, and suggests that other galaxy and/or halo properties may be important.

We have shown that extrapolating the bright-end galaxy–halo connection to the faint end can lead to biased conclusions: the best-fit bright-end SHAM parameters underpredict the clustering at scales $r_p \lesssim 0.75$ Mpc by up to 30% at the faint-end. We also found the parameters of SHAM and its goodness of fit to be functions of both the photometric reduction method (NYU-VAGC, NSA, Sérsic vs Petrosian magnitudes), and especially between the use of r -band luminosity vs stellar mass as input. Lastly, the different selection criteria of the HI galaxies from the ALFALFA survey suggest that a significant alteration to SHAM is required to model the HI–halo connection accurately. A proxy based on peak-to-present virial mass can only recover the HI clustering reasonably well at the cost of a very large scatter. Therefore, a suitable SHAM proxy for HI-selected samples proxy should consider additional halo properties.

ACKNOWLEDGEMENTS

We thank Martha Haynes and Manolis Papastergis for guidance with the ALFALFA data, and Risa Wechsler and Yao-Yuan Mao for comments on the draft.

RS was supported by the Oxford Astrophysics Summer Research Programme. HD is supported by St John’s College, Oxford, and acknowledges financial support from ERC Grant No. 693024 and the Beecroft Trust. MGJ was supported by a Juan de la Cierva formación fellowship (FJCI-2016-29685) from the Spanish Ministerio de Ciencia, Innovación y Universidades (MCIU) during much of this work. He also acknowledges support from the grants AYA2015-65973-C3-1-R (MINECO/FEDER, UE) and RTI2018-096228-B-C31 (MCIU). This work has been supported by the State Agency for Research of the Spanish MCIU “Centro de Excelencia Severo Ochoa” program under grant SEV-2017-0709.

This research made use of the Dark Sky Simulations, which were produced using an INCITE 2014 allocation on the Oak Ridge Leadership Computing Facility at Oak Ridge National Laboratory; we thank the Dark Sky Collaboration for providing access to these simulations. We would like to acknowledge the work of the entire

ALFALFA team in observing, flagging, and source extraction for the ALFALFA catalogue.

DATA AVAILABILITY

The code underlying this article is publicly available at github.com/Richard-Sti/ClusterSHAM. The NSA, NYU-VAGC and ALFALFA catalogues are publicly available. All other data used will be shared on reasonable request to the corresponding authors.

REFERENCES

- Abazajian K. N., et al., 2009, *Astrophys. J. Suppl.*, 182, 543
 Albareti F. D., et al., 2017, *Astrophys. J. Suppl.*, 233, 25
 Baldry I., Glazebrook K., Driver S., 2008, *Mon. Not. Roy. Astron. Soc.*, 388, 945
 Behroozi P. S., Conroy C., Wechsler R. H., 2010, *ApJ*, 717, 379
 Behroozi P. S., Wechsler R. H., Wu H.-Y., 2013a, *ApJ*, 762, 109
 Behroozi P. S., Wechsler R. H., Wu H.-Y., Busha M. T., Klypin A. A., Primack J. R., 2013b, *ApJ*, 763, 18
 Behroozi P., Wechsler R. H., Hearin A. P., Conroy C., 2019, *MNRAS*, 488, 3143
 Bernardi M., Meert A., Sheth R. K., Vikram V., Huertas-Company M., Mei S., Shankar F., 2013, *Mon. Not. Roy. Astron. Soc.*, 436, 697
 Bishop C. M., 1995, *Neural Networks for Pattern Recognition*. Oxford University Press, Inc., USA
 Blanton M. R., Roweis S., 2007, *Astron. J.*, 133, 734
 Blanton M. R., et al., 2005, *Astron. J.*, 129, 2562
 Blanton M. R., Kazin E., Muna D., Weaver B. A., Price-Whelan A., 2011, *AJ*, 142, 31
 Boylan-Kolchin M., Bullock J. S., Kaplinghat M., 2012, *MNRAS*, 422, 1203
 Bryan G. L., Norman M. L., 1998, *ApJ*, 495, 80
 Bullock J. S., Boylan-Kolchin M., 2017, *ARA&A*, 55, 343
 Calette A. R., Rodríguez-Puebla A., Avila-Reese V., del P Lagos C., 2021, *MNRAS*,
 Chauhan G., Lagos C. d. P., Stevens A. R. H., Obreschkow D., Power C., Meyer M., 2020, *MNRAS*, 498, 44
 Chaves-Montero J., Angulo R. E., Schaye J., Schaller M., Crain R. A., Furlong M., Theuns T., 2016, *MNRAS*, 460, 3100
 Conroy C., Wechsler R. H., Kravtsov A. V., 2006, *ApJ*, 647, 201
 Contreras S., Angulo R., Zennaro M., 2020, arXiv e-prints, p. [arXiv:2012.06596](https://arxiv.org/abs/2012.06596)
 DES Collaboration et al., 2021, arXiv e-prints, p. [arXiv:2105.13549](https://arxiv.org/abs/2105.13549)
 Desmond H., 2017, *MNRAS*, 464, 4160
 Desmond H., Wechsler R. H., 2015, *Mon. Not. Roy. Astron. Soc.*, 454, 322
 Desmond H., Wechsler R. H., 2017, *Mon. Not. Roy. Astron. Soc.*, 465, 820
 Dewdney P. E., Hall P. J., Schilizzi R. T., Lazio T. J. L. W., 2009, *IEEE Proceedings*, 97, 1482
 Diemer B., Kravtsov A. V., 2015, *ApJ*, 799, 108
 Durbala A., Finn R. A., Crone Odekon M., Haynes M. P., Koopmann R. A., O’Donoghue A. A., 2020, *AJ*, 160, 271
 Efstathiou G., Ellis R. S., Peterson B. A., 1988, *MNRAS*, 232, 431
 Eisenstein D. J., et al., 2001, *AJ*, 122, 2267
 Esmailzadeh R., Starkman G. D., Dimopoulos S., 1991, *ApJ*, 378, 504
 Feldman H. A., Kaiser N., Peacock J. A., 1994, *ApJ*, 426, 23
 Giovanelli R., et al., 2005, *Astron. J.*, 130, 2598
 Giovanelli R., et al., 2007, *Astron. J.*, 133, 2569
 Guo H., Li C., Zheng Z., Mo H. J., Jing Y. P., Zu Y., Lim S. H., Xu H., 2017, *Astrophys. J.*, 846, 61
 Guo H., Jones M. G., Haynes M. P., Fu J., 2020, *ApJ*, 894, 92
 Hamilton A. J. S., Tegmark M., 2004, *MNRAS*, 349, 115
 Haynes M. P., et al., 2018, *The Astrophysical Journal*, 861, 49
 Hogg D. W., 1999, arXiv e-prints, [pp astro-ph/9905116](https://arxiv.org/abs/astro-ph/9905116)
 Ivezić Ž., et al., 2019, *ApJ*, 873, 111

- Jones M. G., Haynes M. P., Giovanelli R., Moorman C., 2018, *MNRAS*, **477**, 2
- Klypin A., Kravtsov A. V., Valenzuela O., Prada F., 1999, *ApJ*, **522**, 82
- Knebe A., et al., 2011, *MNRAS*, **415**, 2293
- Kravtsov A. V., Berlind A. A., Wechsler R. H., Klypin A. A., Gottlöber S., Allgood B. o., Primack J. R., 2004, *ApJ*, **609**, 35
- Kravtsov A. V., Vikhlinin A. A., Meshcheryakov A. V., 2018, *Astronomy Letters*, **44**, 8
- Landy S. D., Szalay A. S., 1993, *ApJ*, **412**, 64
- Laureijs R., et al., 2011, arXiv e-prints, p. [arXiv:1110.3193](https://arxiv.org/abs/1110.3193)
- Lehmann B. V., Mao Y.-Y., Becker M. R., Skillman S. W., Wechsler R. H., 2017, *Astrophys. J.*, **834**, 37
- Li C., White S. D. M., 2009, *MNRAS*, **398**, 2177
- Li C., Kauffmann G., Fu J., Wang J., Catinella B., Fabello S., Schiminovich D., Zhang W., 2012, *MNRAS*, **424**, 1471
- Lu Y., Yang X., Liu C., Guo H., Xu H., Katsianis A., Wang Z., 2020, arXiv e-prints, p. [arXiv:2008.09804](https://arxiv.org/abs/2008.09804)
- Malmquist G. K., 1920, Meddelanden fran Lunds Astronomiska Observatorium Serie II, **22**, 3
- Malmquist K. G., 1922, Meddelanden fran Lunds Astronomiska Observatorium Serie I, **100**, 1
- Marshall P., Rajguru N., Slosar A., 2006, *Phys. Rev. D*, **73**, 067302
- Martin D. C., et al., 2005, *The Astrophysical Journal*, **619**, L1
- Martin A. M., Giovanelli R., Haynes M. P., Guzzo L., 2012, *ApJ*, **750**, 38
- McGaugh S. S., 2005, *ApJ*, **632**, 859
- McGaugh S. S., Schombert J. M., 2015, *ApJ*, **802**, 18
- McGaugh S. S., Schombert J. M., Bothun G. D., de Blok W. J. G., 2000, *ApJ*, **533**, L99
- Moore B., Ghigna S., Governato F., Lake G., Quinn T., Stadel J., Tozzi P., 1999, *ApJ*, **524**, L19
- Moster B. P., Somerville R. S., Maulbetsch C., van den Bosch F. C., Macciò A. V., Naab T., Oser L., 2010, *ApJ*, **710**, 903
- Moster B. P., Naab T., White S. D. M., 2018, *MNRAS*, **477**, 1822
- Munshi F., Brooks A., Applebaum E., Christensen C., Sligh J. P., Quinn T., 2021, arXiv e-prints, p. [arXiv:2101.05822](https://arxiv.org/abs/2101.05822)
- Navarro J. F., Frenk C. S., White S. D. M., 1997, *ApJ*, **490**, 493
- Norberg P., Baugh C. M., Gaztañaga E., Croton D. J., 2009, *MNRAS*, **396**, 19
- O’Leary J. A., Moster B. P., Naab T., Somerville R. S., 2020, arXiv e-prints, p. [arXiv:2001.02687](https://arxiv.org/abs/2001.02687)
- Pandey S., et al., 2021, arXiv e-prints, p. [arXiv:2105.13545](https://arxiv.org/abs/2105.13545)
- Papastergis E., Giovanelli R., Haynes M. P., Rodríguez-Puebla A., Jones M. G., 2013, *Astrophys. J.*, **776**, 43
- Petrosian V., 1976, *ApJ*, **210**, L53
- Reddick R. M., Wechsler R. H., Tinker J. L., Behroozi P. S., 2013, *ApJ*, **771**, 30
- Reddick R., Tinker J., Wechsler R., Lu Y., 2014, *Astrophys. J.*, **783**, 118
- Rodríguez-Puebla A., Avila-Reese V., Firmani C., Colín P., 2011, *Rev. Mex. Astron. Astrofis.*, **47**, 235
- Ross A. J., et al., 2012, *MNRAS*, **424**, 564
- Saintonge A., Giovanelli R., Haynes M. P., Hoffman G. L., Kent B. R., Martin A. M., Stierwalt S., Brosch N., 2008, *Astron. J.*, **135**, 588
- Schmidt M., 1968, *ApJ*, **151**, 393
- Schneider A., et al., 2016, *JCAP*, **04**, 047
- Sersic J. L., 1968, Atlas de Galaxias Australes
- Skibba R. A., Sheth R. K., 2009, *MNRAS*, **392**, 1080
- Skillman S. W., Warren M. S., Turk M. J., Wechsler R. H., Holz D. E., Sutter P. M., 2014, arXiv e-prints, p. [arXiv:1407.2600](https://arxiv.org/abs/1407.2600)
- Stoughton C., et al., 2002, *Astron. J.*, **123**, 485
- Tinker J. L., et al., 2017, *Astrophys. J.*, **839**, 121
- To C.-H., Reddick R. M., Rozo E., Rykoff E., Wechsler R. H., 2020, *ApJ*, **897**, 15
- Vale A., Ostriker J. P., 2004, *MNRAS*, **353**, 189
- Warren M. S., 2013, arXiv e-prints, p. [arXiv:1310.4502](https://arxiv.org/abs/1310.4502)
- Wechsler R. H., Tinker J. L., 2018, *Annual Review of Astronomy and Astrophysics*, **56**, 435–487
- York D. G., et al., 2000, *AJ*, **120**, 1579
- Zehavi I., et al., 2005, *Astrophys. J.*, **630**, 1
- Zheng Z., et al., 2005, *ApJ*, **633**, 791
- Zwaan M. A., Meyer M. J., Staveley-Smith L., Webster R. L., 2005, *MNRAS*, **359**, L30